Thermal instability and volume contraction in a pulsed microwave N_2 plasma at sub-atmospheric pressure

Thermal instability and volume contraction in a pulsed microwave N_2 plasma at sub-atmospheric pressure

Seán Kelly[1], Alex van de Steeg[2], Ashley Hughes[2], Gerard van Rooij[2] and Annemie Bogaerts[1]

[1] Research group PLASMANT, Department of Chemistry, University of Antwerp, Belgium
[2] Dutch Institute for Fundamental Energy Research (DIFFER), Eindhoven, the Netherlands

E-mail: sean.kelly@uantwerpen.be

Abstract

We studied the evolution of an isolated pulsed plasma in a vortex flow stabilised microwave discharge in N_2 at 25 mbar via the combination of 0D kinetics modelling, iCCD imaging and laser scattering diagnostics. Quenching of electronically excited N_2 results in fast gas heating and the onset of a thermal-ionisation instability, contracting the discharge volume. The onset of a thermal-ionisation instability driven by vibrational excitation pathways is found to facilitate significantly higher N_2 conversion (i.e. dissociation to atomic N_2) compared to pre-instability conditions, emphasizing the potential utility of this dynamic in future fixation applications. The instability onset is found to be instigated by super-elastic heating of the electron energy distribution tail via vibrationally excited N_2. Radial contraction of the discharge to the skin depth is found to occur post instability, while the axial elongation is found to be temporarily contracted during the thermal instability onset. An increase in power reflection during the thermal instability onset eventually limits the destabilising effects of exothermic electronically excited N_2 quenching. Translational and vibrational temperature reach a quasi-non-equilibrium after the discharge contraction, with translational temperatures reaching ~1200 K at the pulse end, while vibrational temperatures are found in near equilibrium with the electron energy (1 eV, or ~ 14,500 K). This first description of the importance of electronically excited N_2 quenching in thermal instabilities gives an additional fundamental understanding of N_2 plasma behaviour in pulsed MW context, and thereby brings the eventual implementation of this novel N_2 fixation method one step closer.

Keywords: N_2 microwave plasma, plasma-based N_2 fixation, pulsed microwave plasma, N_2 dissociation, thermal-ionisation instability, plasma contraction, gas heating.

1. Introduction

Ongoing efforts to mitigate anthropogenic climate change have led to a renewed interest in plasma as a means of chemical feedstock production [4]. Plasma processes typically have very short start-up times, so are readily amenable to intermittent renewable electricity supplies [4], which continue to make up an increasing share of energy grids worldwide [5]. Industrial scale N_2 fixation (NF) via the Haber-Bosch (H-B) process to produce NH_3 dominates artificial fertiliser manufacturing and at present, enables crop yield enhancements which nourish over 40% of the world population [6]. The H-B process is an energy-intensive chemical process, which accounts for 1-2 % of the world's energy production and emits more than 300 million tons of CO_2 [6]. Application of plasma technology offers the potential of an energy-efficient CO_2 free NF alternative.

Plasma-based NF can be carried out in pure N_2 gas streams (with subsequent reaction to produce NO or NH_3) or in N_2/O_2 or N_2/H_2 or N_2/H_2O mixes where both gaseous and liquid H_2O can be employed [7-13]. Owing to the exceptional stability of the N_2 triple bond, interrogation of efficient routes for N_2 dissociation remains a key hurdle to advancement in these fixation processes.

Microwave (MW) generated plasmas offer desirable characteristics [14] of high electron densities with relatively low mean electron energies (e.g. in the range ~1-3eV), conditions which can exploit the most efficient dissociation route via electron impact vibrational excitation for atmospheric molecular gases such as N_2 [10]. Investigations in the early 1980s by Asisov et al. [15, 16] employing a low pressure Electron Cyclotron Resonance (ECR) MW discharge in N_2/O_2 mixes reported encouraging NO_x production levels of 14% at energies of 300 kJ/mol (SEI = 3.1 eV/molecule) [6]. Many modern efforts have however focused on (near) atmospheric pressure discharges, given the impracticalities of employing low pressure for gas conversion.

Continuously powered molecular MW plasmas at atmospheric and sub-atmospheric pressure are typically categorised as 'warm' plasmas [4, 15] ($T_g \geq 3000$ K) with significant energy directed to gas heating. Generally, this leads to conditions where the most efficient vibrational route to molecular dissociation [10] is suppressed due to thermalising of the vibrational distribution function (vibrational-translational (V-T) induced depopulation of higher vibrational states [14]). Strategies to limit gas heating have therefore received particular attention.

One heat-limitation strategy for MW plasmas involves the use of supersonic flows operating at/above ambient pressures [15]. Forcing a gas into a constriction, such as achieved using a de Laval-type nozzle exploiting the Venturi principle [17], can result in supersonic acceleration downstream, leading to significant gas cooling. This can be imagined as a sort of 'spatial pulsing' which limits the gas to a short residence time in a plasma state with the additional benefit of the gas consuming its own internal energy as it breaks the sound barrier. Recent modelling investigations in CO_2 have shown upper efficiency limits for this approach at ~ 40% [18]. Achieving both high conversion and energy efficiency indeed remains challenging however. The short residence time of the gas in the plasma region limits population of higher vibrational levels. The sharp temperature and pressure rise during the post-constriction shockwave formation can also quickly depopulate higher vibrational levels and increase recombination. Thermal choking at higher power densities was also found to be an important scalability hurdle for this heat limitation strategy [18].

The use of pulsed-powering also presents an interesting strategy for heat limitation in MW plasmas [19-23]. In this case, the feed gas is limited to plasma formation in time (power on/off). Modern developments in solid state power supplies have enabled unprecedented control of pulse conditions [24], overcoming many challenges with power modulation of the 'traditional' magnetron power supplies [25]. Further, vortex gas flows are now frequently employed to stabilise MW plasmas in gas conversion studies under near-atmospheric conditions [17, 26-29]. Such swirling flows stabilise discharge operation by isolating the discharge from the container (e.g. quartz tube). This reduces thermal loads on the walls, which is beneficial to both prevent damage and maintain discharge stability.

Recent investigations via iCCD imaging by Van Alphen et al. [21] studied pulse conditions in an N_2 vortex stabilised MW plasma at 25 mbar. Operating at conditions synonymous with a diffuse discharge [27, 29], they found that upon ignition, the plasma gradually expanded (to eventually reach a steady diffuse volume) from a small spherical volume. Given an appropriate choice of pulse conditions, they unravelled optimum power pulse widths and inter-pulse periods, which balance the population of vibrational levels with gas cooling. Promising efficiencies were reported [21], however, conversion levels remained low. A rise in pressure or power (i.e. increasing the ionisation fraction) is therefore motivated to address intensified and more industrially relevant conditions. Higher ionisation fractions are however well known to result in a mode change, in which the discharge volume can become significantly contracted and heated due to the onset of thermal-ionisation instabilities with significantly different plasma parameters compared to diffuse mode discharges [27-31].

Ionisation overheating arises due to the exponential dependence of ionisation events following an increase in gas temperature [32]. Gas heating decreases the gas density (N) (under isobaric conditions) which propagates a feed-back loop of further ionisation and heating. Thermal-ionisation instabilities typically result in discharge contraction, a characteristic feature of high-pressure discharges, where non-uniform gas heating, changing dielectric properties, chemical dynamics and self-compression (via Lorentz forces) of the resulting plasma filament play a role in containing the discharge. Ignition and instability conditions in a pulsed MW scenario occur within each pulse repetition. Understanding thermal-ionisation instabilities in this context is thus more prominent compared to continuously powered discharges. Controlling and exploiting thermal ionisation conditions is therefore key for future commercial realization of (near) atmospheric pressure plasma N_2 fixation processes. This is particularly essential for establishing process intensification where higher power densities are desirable.

Pulsed power MW plasmas in N_2 at sub-atmospheres have been previously studied by Baeva et al. [20, 33] confirming the high level of vibrational excitation present. These studies were limited to rather mild power absorption conditions and did not report the occurrence of thermal instabilities or high ionisation fractions. Modelling by Tatarova et al. [34] in continuous powered surface wave sustained discharges in N_2 demonstrated the importance of super-elastic heating of the electron energy distribution function (EEDF) at higher ionisation fractions. The radial contraction in various gases under continuous MW powering has been correlated to thermal conductivities [30, 35] emphasising the importance of gas heating. Golubovskii et al. [36] argue the key role of non-uniform gas heating in noble gas discharges where a denser central portion of the plasma will usually have more populated electron energy distribution function (EEDF tail) leading to higher ionization rate coefficients and further contraction. High heating rates have been observed in various N_2 and N_2/O_2 molecular discharges, with indications of the key role of electronically excited N_2 molecules [30, 37, 38]. Indeed, during the ignition stage in N_2

discharges under continuous powering, electronically excited N_2 species were acknowledged to contribute briefly but significantly to gas heating in both direct current (DC) and continuously powered MW discharges [37, 39, 40].

Recent work on fast gas heating in N_2 (i.e. in which the increase in gas temperature occurs on timescales much shorter than vibrational-vibrational (VV) and vibrational-translational (VT) reactions) has revealed the importance of metastable and electronically excited species in rapid heat deposition in pure N_2 discharges [41-44]. Lepikhin et al. [41] investigated fast heating in N_2 for nanosecond (ns) pulsed capillary dishcarges at 27 mbar and low flows conditions with relatively high reduced electric fields (E/N) ranging 100-300 Td. The authors outlined the important contributions of electronically excited species of both molecular and atomic nitrogen in the high heating rate. Shkurenkov et al. [42] studied the energy balance in pulsed ns discharges in N_2 at ~130 mbar, and demonstrated the rise in gas heating occurs in two stages: rapidly due to energy pooling and quenching of molecular and atomic species and a slower heat release due to vibrational relaxation. Nudnova et al. [43] also noted the significance of heat released by quenching of electronically excited N_2 in sub atmospheric pressure ns surface barrier discahrges. Modelling work by Pintassilgo et al. [44] correlated N_2 metastable quenching to the heating rates found in lower pressure (~3 mbar) glow discharges of Gordiets et al. [45]. Numerical calculations by Aksihev et al. [46] at atmospheric pressure in a constricted glow discharge demonstrated an non-equilibrium between vibrational and gas temperatures is sustained at low reduced fields (< 20 Td) via a strong coupling between vibrationally and electronically excited molecular species. Extensive coverage of the fundamental kinetics of N_2 plasmas by Capitelli et al. [47] emphasise the profound role of electronic excitation on discharge properties. Detailed thermo-chemical interrogation of pulsed MW discharges has to date however been limited in the context of pure N_2 discharges.

Future commercial realisation of N_2 fixation applications using pulse-powered MW discharges requires a detailed understanding of ignition and instability behaviour given the prominence of such phenomena at higher power densities and (near) ambient pressures. However, the dynamics of how vibrational, electronically excited and metastable chemistries impact the occurrence of thermal-ionisation instabilities remains at present largely unclear. Given the frequent occurrence of ignition events in pulsed discharges (i.e. during every pulse), thermo-chemical scrutiny of this dynamic is required to progress understanding. Motivated by this, our paper focuses on a detailed analysis of the ignition of a single power pulse in the context of a vortex flow stabilised MW plasma operating in N_2 at sub-atmospheric pressure (25 mbar).

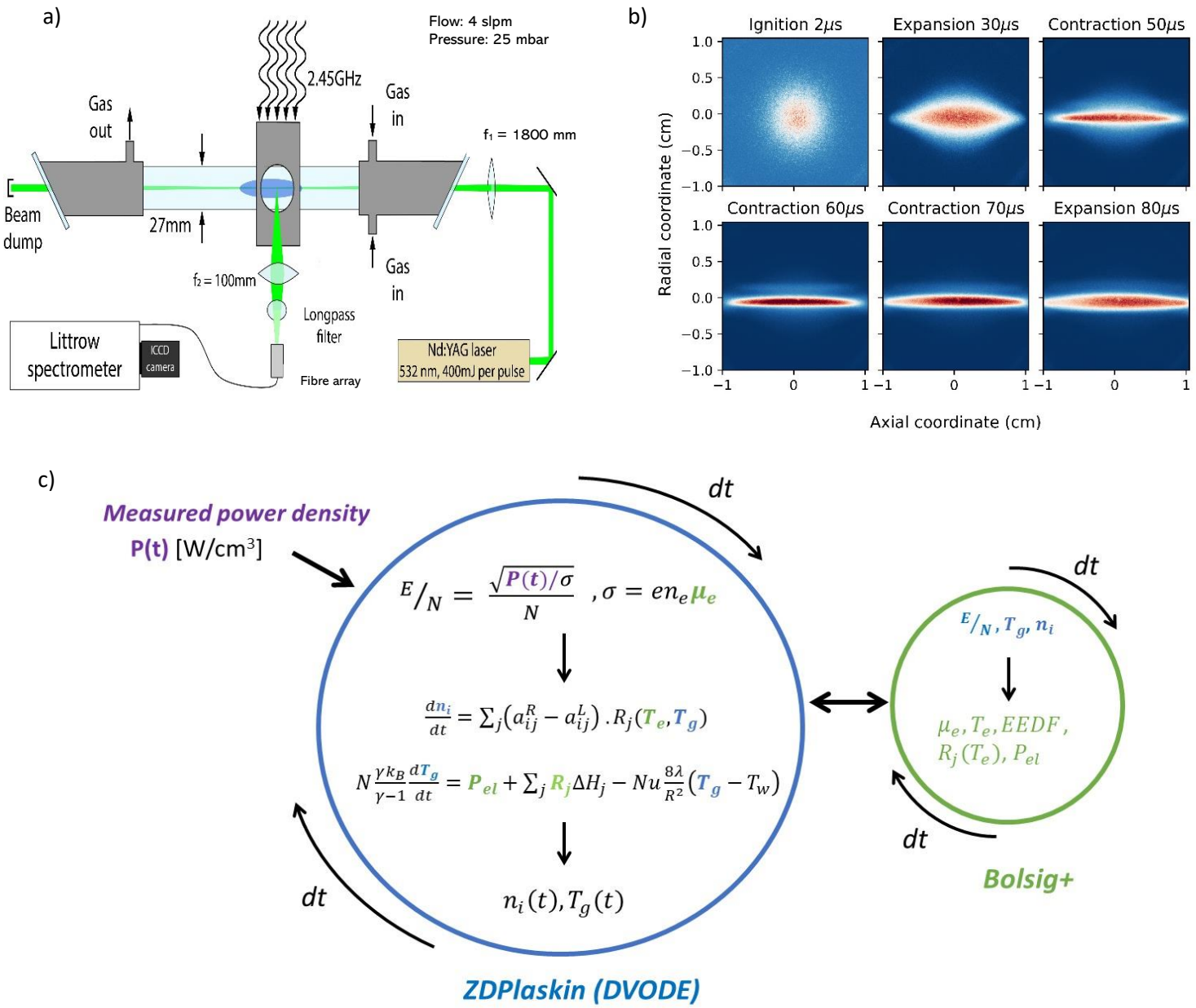

Figure 1 a) *Experimental setup and diagnostic arrangement, and* ***b)*** *Sequence of iCCD images of dynamic phase of pulse duration, showing initial discharge expansion (2-30 μs), followed by contraction to the skin depth (50-70 μs), and finally expansion (>80 μs).* ***c)*** *Overview of the numerical solution scheme for the 0-D model employing ZDPlaskin [1] which incorporates the DVODE code [2] for ODE integration and Bolsig+ [3] to solve the Boltzmann equation at each time step. An experimentally determined power density [W/cm^3] is coupled externally to enable solution via the reduced electric field E/N.*

2. Experimental and computational details

2.1 MW reactor and laser diagnostic details

0D kinetic modelling is combined with iCCD imaging and laser scattering diagnostics (Raman and Thomson) to give a detailed account of gas heating and chemical dynamics. **Figure 1** a) presents a

diagram of the reactor setup and diagnostic arrangement. An isolated MW discharge pulse is established by power pulsing at a relatively 'slow' frequency (30 Hz in this case) with a relatively high gas flow rate (4 slpm). This ensures that the residence time of the gas in the plasma region is significantly shorter than the inter-pulse period (i.e., ~5 ms vs 33 ms (30 Hz)), thus ensuring that any gas molecule will only see one pulse when passing through the discharge2.1 MW reactor and laser diagnostic details

The experimental layout is schematically shown in **Figure 1** (a). A solid-state MW power source (Ampleon) applies 200 µs, 800 W peak power MW pulses via waveguides to a 27 mm inner diameter quartz tube, where the plasma is generated. An EH tuner and adjustable short are used to tune the electrical field to optimal conditions for electrical breakdown. Perfect impedance matching could not be realized for the entire duration of the plasma pulses due to variations in plasma impedance, an effect of the altering electron density also observed by Baeva et al. [33]. Tangential gas injection leads to a swirl flow in the tube, which stabilises the plasma and ensures the location of breakdown is repeatable.

A 30 Hz, frequency doubled Nd:YAG laser (SpectraPhysics GCR-230) of 400 mJ per pulse and 8 ns pulse duration is focused into the centre of the plasma. A 100 mm focal distance lens collects and focuses the scattered light into a fibre array. The fibres relay the scattered light into a 50 µm entrance slit of a 1 m focal distance custom built Littrow-configuration spectrometer equipped with an 1800 l/mm grating, yielding a dispersion of 0.012 nm/pixel. The spectrally resolved image is captured by an em-ICCD (Princeton Instruments PiMax4) camera. Rejection of stray light, a crucial aspect in laser scattering studies, is achieved by placing a sharp-edge long-pass filter (Semrock RazorEdge) in front of the fibre array.

The plasma system is placed upon a translation stage and thus allows radial movement of plasma with respect to laser. This feature is utilised to measure in the centre of the plasma and 1 and 2 mm radially outward. Since a fibre array instead of a single fibre is used, the iCCD array obtains a spatial axis displaying tens of fibres. Sensitivity is increased by binning along this axis, effectively leading to spatial averaging in the axial direction of 15 mm.

Vibrational and rotational temperatures in the inhomogeneous N_2 plasma are revealed through vibrational Raman scattering, the diagnostic of choice because of its high temporal and spatial resolution. The strong Q-branches of the different vibrational levels are spectrally separated by the anharmonicity to readily yield vibrational populations. Rotational temperatures are simultaneously obtained through the asymmetry of the Q-branches. At low rotational temperatures, the asymmetry of the Q-branches and instrumental broadening overlap partly, resulting in relatively high uncertainty at low gas temperature. At higher gas temperatures, the asymmetry becomes more apparent, but signal intensity Nevertheless, the diagnostic gives a good indication of the evolution of the rotational temperature over the pulse. Previous work on N_2 continuous plasma by Gatti et al. [48] contains further details on the application of vibrational Raman scattering, while general features of the experimental setup can be found in [27].

A least-squares fit with free parameters T_{rot}, $T_v^{0,1}$ and $T_v^{1,5}$ minimizes the residual between experimental data and custom-made fitting function. The mathematical formulations of vibrational Raman scattering incorporated in this function are defined in [48, 49]. One rotational temperature is assumed for all vibrational levels and the vibrational temperature $T_v^{1,5}$ assumes a Boltzmann distribution between the observed levels 1 to 5.

Rotational temperatures serve as a proxy for the gas temperature, a natural assumption following from the very fast rotation-translation relaxation times [50]. Vibrational populations up until v = 5 are measured, where the distribution of the levels is seen to deviate from a Boltzmann distribution. Two vibrational temperatures are then defined, inspired by works of Lo et al. [51] and Montello et al. [52]: $T_v^{0,1}$ belonging to the ratio of populations between v=0 and v=1 and $T_v^{1,5}$, belonging to the remaining observed vibrational states, 1 to 5.

Vibrational and rotational temperatures could only be resolved in the first half of the pulse; after 50µs a combination of strong plasma emission of the first positive system ($N_2(B^3\Pi_g - A^3\Sigma_u^+)$) and an increase in gas temperature cause a sharp decrease in sensitivity.

Recent work of Van de Steeg et al. [53] reports a process of obtaining Thomson scattering in N_2 plasma by capitalising on the polarisability of the rotational Raman signature. While increasing gas temperature leads to decreased sensitivity to (vibrational) Raman scattering, it also causes increased sensitivity of Thomson scattering. Therefore, Thomson scattering signatures could be retrieved at t = 70 µs. No complete Thomson scattering trace could be retrieved through the pulse due to an initially too intense rotational Raman signal (t = 0 to 60 µs), and a too strong emission of the first positive system $\triangle$v = -5 band in the remainder of the pulse. Nevertheless the Thomson data allows for valuable verification of modeled electron properties.

2.2 0D kinetic modelling details

A 0D model is employed using ZDPlaskin (Zero-Dimensional Plasma Kinetics) solver [1]. An overview of the simulation scheme is given in **Figure 1** c). The time evolution of the species densities including electron, charged and neutral species is calculated by taking into account the various production and loss terms by chemical reactions:

$$\frac{dn_i}{dt} = \sum_j \left(a_{ij}^R - a_{ij}^L\right) . R_j \qquad (1)$$

$$a_A\, A + \; a_B B \; (+\Delta H) \xrightarrow{k_j} a_c C + \; a_D D \; (+\Delta H) \qquad (2)$$

$$R_j = \; k_j \prod_l n_l^L \qquad (3)$$

Here n_i represents the density of species i and a_{ij}^R and a_{ij}^L are the stoichiometric coefficients of species i on the right-hand and left-hand side of reaction j. Reactions have the general form of equation (3) where A, B, C and D are the species and a_A, a_B, a_c, and a_D their stoichiometric coefficients. ΔH in equation (3) represents the possible energy change during the reaction. The reaction rate R_j is shown in equation (4), where k_j is the reaction rate coefficient of reaction *j* and $\prod_l n_l^L$ represents the product over left-hand side reactants.

The reduced electric field E/N, where N is neutral gas density, is calculated from a specified power density.

$$E/_N = \frac{\sqrt{P/\sigma}}{N} \quad (4)$$

Here σ is the plasma conductivity, which is calculated using the electron mobility $\mu_e\ (E/N)$ (output from the Boltzmann solver [1, 3]) via $\sigma = en_e\mu_e$ where e is the electron charge. The power density P is derived from experimental measurements of the absorbed power (i.e. forward – reflected power) combined with determination of the plasma volume using iCCD imaging (see details below). A cylindrical volume is assumed here to approximate the discharge volume [21] using measurements of the plasma length and width from the 2D profiles shown in figure 1 (b). This approximation is consistent with vortex stabilised discharges where the plasma is contained within the inner vortex flow, elongating along the direction of the flow (i.e. along the plasma length) [21, 28, 29].

The gas temperature is solved in the model on each time step. Values of the enthalpy contributions from the chemistry, heat losses to the walls and the dynamic heat capacity taking account of the gas mixture are accounted for on each time step. The radially averaged gas temperature T_g (the gas temperature is assumed to have a parabolic profile) in our axially homogeneous tube is calculated by considering the time dependent gas thermal balance equation under isobaric conditions [54, 55] as:

$$N\frac{\gamma k_B}{\gamma-1}\frac{dT_{gas}}{dt} = P_{el} + \sum_j R_j\Delta H_j - Nu\frac{8\lambda}{R^2}\left(T_g - T_w\right) \quad (5)$$

Where γ is the specific heat ratio (i.e., the ratio of the isobaric and isochoric heat capacity which is calculated assuming a mixture of an ideal diatomic and monatomic gas [21]); k_B is the Boltzmann constant, P_{el} is the power density due to elastic collisions of electrons with heavy neutrals (an output from the Boltzmann solver [1, 3]); R_j is the rate of reaction j with associated enthalpy contributions of ΔH_j, λ is the gas thermal conductivity (with $\gamma(T_g)$ [21, 56] data from [57]), T_w is the wall temperature (set to 300 K), and R is the reactor radius (see **section 2.1**). The non-dimensional term $'Nu'$ in **equation 5** is the the Nusselt number, which is defined as the ratio of convective to conductive heat transfer to the tube walls. For Nu = 1, heat loss is purely conductive (i.e., diffusive) accounting for a laminar flow or stagnant situation. Values of Nu > 1 characterise enhanced convective thermal losses typical of the turbulent flow conditions in vortex-sustained MW discharges of interest here [58]. The Nusselt number can be expressed as $Nu = \frac{\alpha.R}{\lambda}$ where $\alpha\ [\frac{K}{cm^2\ s}]$ is the convective heat transfer coefficient (which encompasses both advective and diffusive heat transport), $\lambda\ [\frac{K}{cm\ s}]$ the thermal conductivity (i.e., diffusive heat transport) and $R\ [cm]$ the tube radius as the representative length scale. The power loss via heat transfer to the walls is therefore formulated equivalently as $\frac{8\alpha}{R}\left(T_g - T_w\right) = Nu\frac{8\lambda}{R^2}\left(T_g - T_w\right)$ [54, 58]. A fully resolved turbulent model of the reacting flow is highly computationally intensive and therefore beyond the scope of this work [26]. A Nusselt number in range $Nu{\sim}100 - 1000$ is typically advised for well-developed turbulent flows [59]. Recent estimates of this contribution in similar MW vortex plasma discharges suggest a choice of $Nu{\sim}100$ [60]. Thus this value is employed here as a first order approximation of turbulent enhanced heat losses. It must also be noted that in equation 5 (LHS) the fluid related term "γ kB/(γ − 1) dT/dt" is equivalent to a "NC_p dT/dt" formulation given by γ = C_p/C_v.

The ratio γ is dynamically updated throughout the (isobaric) simulation based on the changing gas mixture during conversion.

The fluid velocity is incorporated via a plug flow approximation. On each time step the relation $dx = v\ dt$ advances the gas plug. This assumes the velocity v is uniform across the tube diameter. Changes in particle densities due to heat and stoichiometry changes are accounted for dynamically by taking account of the initial fixed mass flow Q_{inlet} with the assumption of isobaric conditions P_0. The velocity is given by:

$$v = \frac{Q_{inlet}}{\rho\, \pi\, r_{tube}^2}\ ,\ \rho = \sum_i m_i n_i\ \ ,\ \sum_i n_i = P_0/k_B T_g \qquad (6)$$

Where Q_{inlet} is the fixed mass flow at the inlet, $\rho(t)$ is the mass density for species with mass m_p and the total number density $\sum_i n_i\,(t)$ with (radially averaged) gas temperature $T_g(t)$. The mixture fraction along with the gas temperature and the reduced electric field are continually updated in calls to Bolsig+ as shown in **Figure 1** c).

The N_2 chemistry employed here (58 species, ~6000 reactions) is detailed in [21]. Key additions for this paper include the incorporation of enthalpy contributions from so-called 'pooling reactions' involving $N_2(A^3\Sigma)$ self-quenching to $N_2(B^3\prod)$ and $N_2(C^3\prod)$ [37, 39, 40, 61, 62] and a $N_2(B^3\prod)$ pooling reaction recently proposed by Lepikhin et al. [41]. Note here the same rate coefficient is taken for $N_2(A^3\Sigma)$ self-quenching as for $N_2(B^3\prod)$ self-quenching [41]. To characterise heat release in the quenching of electronically excited $N_2(B^3\prod)$ with N_2 enthalpy contributions are incorporated from [63]. For atomic nitrogen species, a $N(^2P)$ associative ionisation reaction (i.e. $N(^2P) + N(^2P) \rightarrow e + N_2^+$) [64, 65] is added. Further an increased $N(^2P)$ recombination rate coefficient (i.e. $N(^2P) + N_2 \rightarrow N_2 + N(^4S)$) to match recent reports [64, 65] is also included. A (gas) temperature sensitive rate coefficient for $N(^2D)$ deexcitation to $N(^4S)$ [66] is included to appropriately capture the $N(^2D)/N(^4S)$ population balance [42] under the relatively high temperatures found here. The enthalpy contribution from electron-ion recombination for the key ionic species N_2^+ is included from [41, 67]. Elastic collisions for $N(^2P)$ and $N(^2D)$ excited atomic nitrogen species (along with $N(^4S)$ elastic collisions in our earlier work [21]) have also been included here [68, 69]. For the heavy particle reactions, the rate coefficients are adopted from earlier work [10, 21, 70], whereas the rate coefficients for the electron impact reactions are calculated using the Boltzmann solver BOLSIG+ [3] built in ZDPlasKin. BOLSIG+ uses a two-term approximation to calculate the electron energy distribution function (EEDF). From the EEDF the mean electron energy and the different electron impact rate coefficients are obtained [3]. Super-elastic collisions for both vibrational and electronically excited states have been included here, as in previous reports [21]. The impact of vibrationally and electronically excited species on the electron energy distribution function is calculated explicity using a detailed balancing based on the forward reaction cross section data. An explicit vibrational and electronic excitation scheme for N_2 is therefore employed here with regards to EEDF calculations in BOLSIG+ (i.e. no automatic inclusion of super-elastic collisions is enabled in lieu of the complete kinetics incorporated here). The EEDF is solved at each time step of the ZDPlaskin solution by calling Bolsig+ to solve the stationary Boltzmann equation [3]. The validity of this quasi-stationary approach is considered with regard to the relaxation time for elastic collisions impacting on the isotropic components of the two-term boltzmann equation [71]. The electron-N_2 collision frequency ν_{e-N_2} is found to typically range between 5 and 20 GHz over the power pulse (see **Figure 2** c). Employing a median collision frequency of $\nu_{e-N_2} \sim 12.5\ \mathrm{GHz}$, an order of magnitude estimate for the momentum relaxation timescale for the electron energy distribution function (τ_{em}) can be given [71]

by the relation $\tau_{em} \approx \nu_{e-N_2}^{-1} {M_{N_2}}/{2m_e} \approx \frac{1.3x10^4}{12.5x\ 10^9} \approx 1\ \mu s$. Such a timescale is reasonably disparate compared to the power pulse period of 200 μs, providing some un-coupling of timescales to capture aspects of the EEDF temporal behaviour. Indeed, coupling with a time-resolved EEDF solution would be an interesting future advancement [72], but this is currently beyond the scope of this work. The ZDPlaskin implementation of Bolsig+ uses by default a caching strategy to improve solution times of the Boltzmann equation at every time step. This only solves the EEDF if key parameters have shifted considerably from time step to time step. No significant differences were found between solutions employing this caching mechanism compared with solutions without this function enabled (i.e., conditions 'with' and 'without' the caching mechanism turned on were simulated in this context). Electron-electron collisions are accounted for above ionization fractions of 10^{-5} in Bolsig+ via ZDPlaskin settings (levels which are indeed reached during the discharge pulse).

Wall losses are incorporated by inclusion of a loss rate for each species based on ambipolar and neutral diffusion coefficients coupled with characteristic diffusion lengths [37]. Diffusion coefficients for neutral species are calculated using a fitting parametrized by the gas temperature [73] while surface loss probabilities for vibrationally excited molecular species, electronically excited molecular species and electronically excited atomic species follow [37]. Ion diffusivity is incorporated with data from [74] parametrized on the reduced electric field. Further details of the particulars of the formulation employed here can be found in [37]. Note that, surfaces losses were not found to have a significant impact as a destruction avenue for the key species when considered over the pulse period (see **Appendix 1)**, probably due to the relatively short time scale considered here**.** Prediction of any increased impact of surface losses over longer pulse and residences times is not interrogated here.

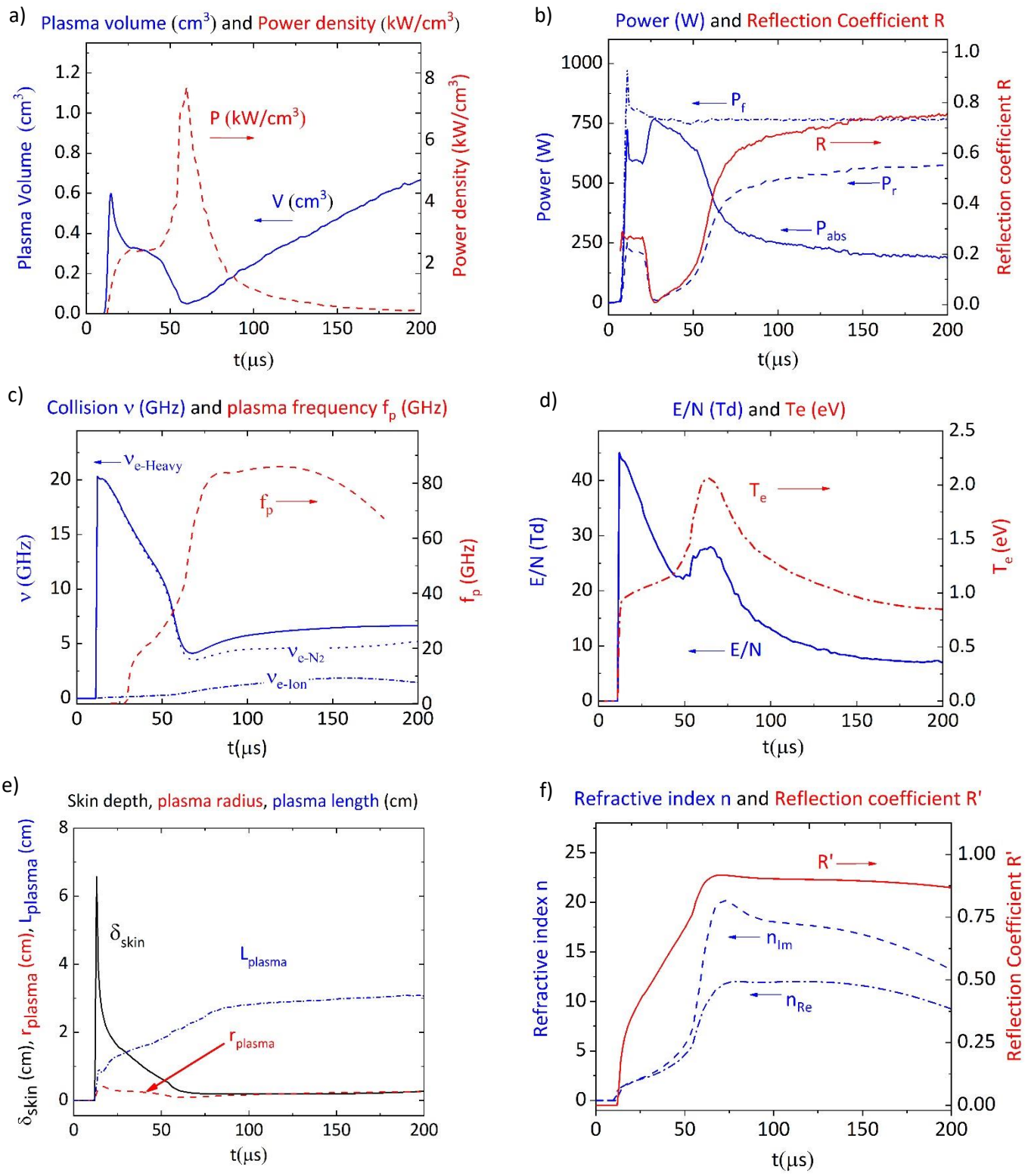

Figure 2 a) *Plasma volume (cm^3) inferred from iCCD images as shown in figure 1, and corresponding calculated power density (kW/cm^3).* ***b)*** *Measured applied power (W): forward (P_f), reflected (P_r) and absorbed power (P_{abs}), and measured reflection coefficient, where R = P_r/P_f.* ***c)*** *Collision frequency (GHz), where total collision frequency $\nu_{e-Heavy} = \nu_{e-N2} + \nu_{e-Ion}$ is the summation of electron-N_2 (ν_{e-N2}) and electron-Ion (ν_{e-Ion}) collision frequencies, and plasma frequency f_p (GHz).* ***d)*** *Calculated reduced electric field E/N (Td) and electron temperature T_e (eV) from the model.* ***e)*** *Skin depth $\delta_{skin}(cm)$, plasma length L_{plasma} and plasma radius r_{plasma} as measured from iCCD images shown in Figure 1.* ***f)*** *Plasma refractive index (real and imaginary parts) where $n = n_{Re} + n_{Im}$ and model-calculated reflection coefficient R'.*

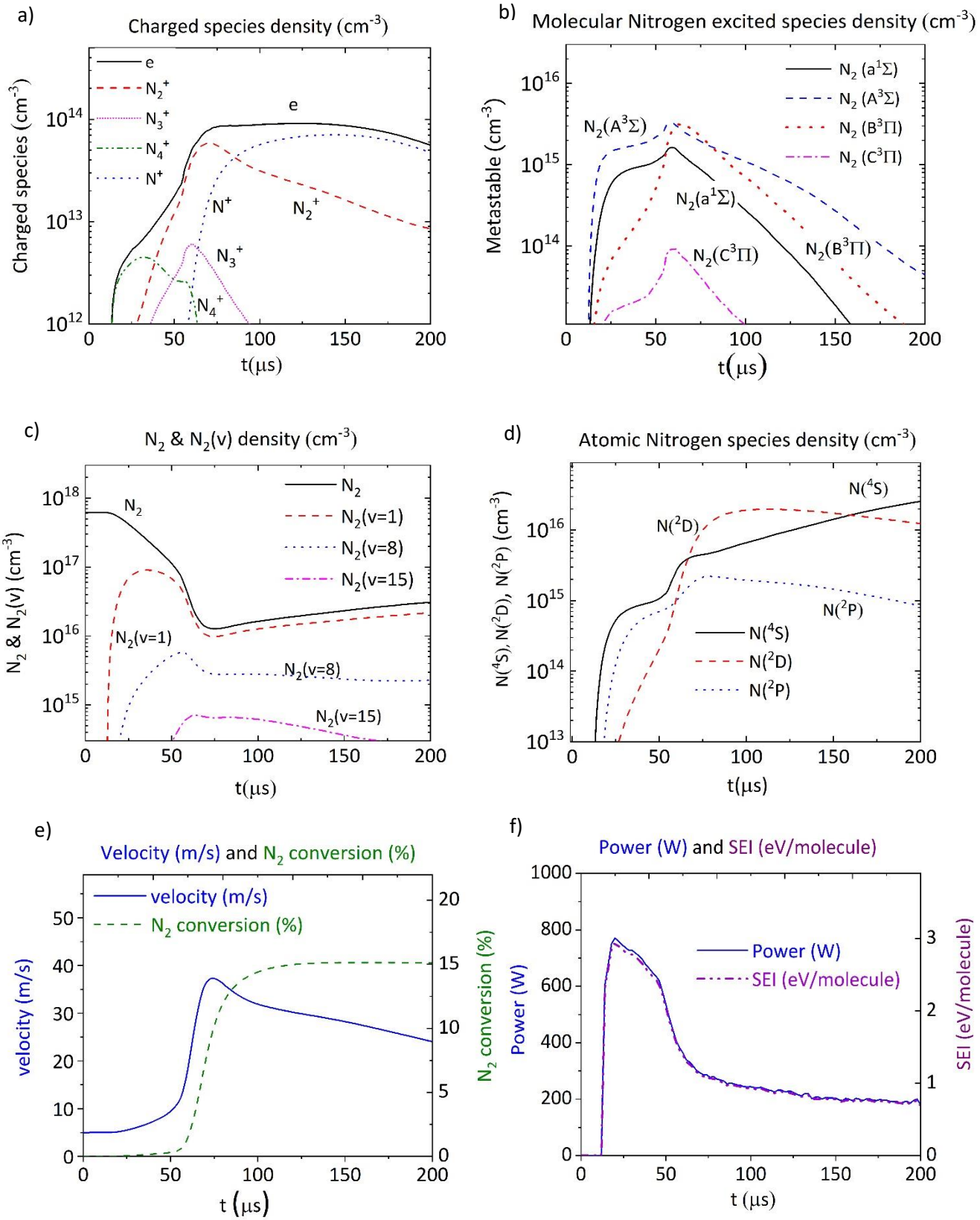

Figure 3 a) *Charged species densities (cm^{-3}).* ***b)*** *Molecular Nitrogen excited species densities (cm^{-3}).* ***c)*** *N_2 and $N_2(v)$ densities (cm^{-3}).* ***d)*** *Atomic N species densities (cm^{-3}).* ***e)*** *Gas velocity (m/s) and N_2 conversion (%).* ***f)*** *Absorbed power (in units of W or J/s) from external power supply and the corresponding Specific Energy Input (SEI; eV/molecule).*

3. Results and discussion

3.1 Plasma volume, collisional dynamics and dielectric properties

Figure 1 b) presents a temporal sequence of iCCD images of the discharge. The associated plasma volume shown in **Figure 2** a) is calculated using the extracted plasma radii and lengths shown in **Figure 2** e) for the absorbed power conditions shown in **Figure 2** b). The optical emission is found to have a Gaussian distribution in its radial and lateral intensity variation (i.e., via pixel intensity measurement across the plasma axis). The plasma boundary is chosen as the full width at quarter maximum (FWQM) of the central peak emission. As the choice of this boundary is quite arbitrary, simulations for a range of n^{th} maxima of the full width were considered. The choice of the FWQM was found to coincide well with the calculated skin depth (shown in **Figure 2** e) and the measured heating rates (**Figure 4**), however, the model cannot predict '*ab-initio*' such parameters. This leads to the necessity for an approximation here which has a significant impact on the estimation of power density, given the sensitivity of the plasma radius in calculating the cylindrical plasma volume. Following ignition, the plasma volume quickly expands to a prolate shape remaining relatively diffuse until t ~ 50 µs when a volume contraction phase (t ~ 50-70 µs) occurs, marking the onset of a thermal-ionisation instability (gas temperatures are discussed in **section 3.2**). At t ~ 70 µs the discharge stabilises and begins expanding again throughout the remainder of the pulse duration (t ~ 80-200 µs).

Figure 2 a) also illustrates the accompanying calculated power density (right). During the volume contraction, a large increase in the power density (up to 8 kW/cm^3) coupling to the plasma occurs in the interval 50-70 µs, when the plasma length, radius and corresponding volume are found to decrease abruptly. An eventual return to pre-instability power densities (<< 1 kW/cm^3) occurs after t ~ 70 µs for the remainder of the pulse, as shown in **Figure 2** a).

The volume contraction and increased gas temperatures (see below) have a significant effect on the plasma characteristics. The plasma frequency (**Figure 2** c) is ~5 GHz at t < 50 µs, jumping to ~ 80 GHz during the power density spike (50 µs < t < 70 µs), before it decays to ~ 60 GHz later in the pulse. The electron-neutral collision frequency ν_{e-N2} shows contrary behaviour to the plasma frequency, dropping considerably at t > 50 µs, despite a large increase in the ionisation fraction (which changes from ~ 10^{-5} at t < 50 µs to ~10^{-3} at t > 100 µs – see **Figure 3** below). This ν_{e-N2} reduction is due to the large drop in the neutral gas density (~1-2 orders of magnitude - **Figure 3**) under isobaric conditions as the gas temperature increases. This marks two distinct discharge modes, before and after the instability onset, where $\nu_{e-Heavy} > f_p$ (t < 50 µs) and $f_p > \nu_{e-Heavy}$ (t > 70 µs). The changing ratio of f_p and $\nu_{e-Heavy}$ results in significantly different dielectric properties for the discharge before/after the thermal instability. As a first approximation, the absorbed power is locally dissipated by electron collisions with heavy species [75]. Changes in the dielectric properties and reflected power (further discussion below) can, therefore, be understood corresponding to the changing electron-neutral collision frequency $\nu_{e-Heavy}$ and plasma frequency f_p as shown in **Figure 2** c).

The electron temperature in **Figure 2** d) is relatively constant (~ 1 eV) up to 50 µs, but rises considerably to ~ 2 eV during the thermal instability, followed by a gradual drop towards ~1 eV near the end of the pulse. The higher plasma frequency/electron density during the thermal contraction allows detection of a Thomson scattering signal from the scattering light (see **section 2.1**) at t ~ 70 µs. Measured values of $f_p \geq 28\ GHz$ ($n_e \geq 10^{13}\ cm^{-3}$) and $T_e \sim 1.4\ eV$ compare reasonably with the calculated values shown in figures **Figure 2**(c, d), providing some corroboration with modelling efforts. Unfortunately, the elusiveness of the signal in our setup prevented temporal capture throughout the pulse. The reduced electric field shown in **Figure 2** d) steadily decreases from 40 to 10 Td throughout the pulse (further details below on the consequences of this).

The radial variation of the plasma (r_{plasma}) is shown in **Figure 2** e). The temporal trend is found to be similar to the axial variation (L_{plasma} shown in the same panel) with an initial expansion following ignition, before an abrupt drop at 50 µs due to high gas heating. Notably, the radial expansion is maintained here at values close to the skin depth [29, 30] after thermal instability onset. Indeed, continuously powered vortex stabilised MW discharges in CO_2 have recently been reported to form a contracted filament with the radial expansion approximated to the skin depth [29]. Under the pure N_2 conditions discussed here, we see that the extent of the radial plasma contraction can lie well below the skin depth in the initial ignition phase of the pulse [30]. Further, recent reports in similar CO_2 and CH_4 pulsed-powered MW experiments [53] do not show this at 25 mbar while in continuously powered vortex stabilised MW CO_2 discharges a contracted discharge is found to occur only at > 150 mbar [27-29].

The axial elongation of the discharge (i.e. in the direction parallel to the tube walls), also shown in **Figure 2** e), is due to surface wave propagation [75-77]. A surface wave plasma is sustained by the propagation of an electromagnetic wave axially outwards from the centre of the waveguide, which transfers its energy to the plasma via kinetic interaction with electrons. Generally, the axial variation in plasma parameters is far less pronounced compared to the radial variation [29, 30, 35]. The threshold plasma frequency f_p for surface wave propagation is given by [76, 78, 79].

$$f_p > f\left(1 + \epsilon_{quartz}\right)^{\frac{1}{2}} \qquad (7)$$

Taking a relative permittivity for the quartz tube as $\epsilon_{quartz} \sim 3.8$ we find the threshold plasma frequency condition of $f_p \sim 5.4$ GHz. In **Figure 2** c) we see that plasma frequency conditions above this threshold are satisfied throughout the pulse duration, except in the first 40 µs. At t > 50 µs, f_p is sustained substantially above this threshold. During the thermal instability (50 µs < t < 70 µs) the axial attenuation of MW power is found to be significantly disrupted locally at the location of the tube centre and waveguide intersection (i.e. x =0 in **Figure 1** a)). The contraction in the axial expansion (L_{plasma}) as shown in **Figure 2** e) can, therefore, be understood by a temporary and localised increase in the surface wave attenuation. In **Figure 2** c) we see at 50 µs < t < 70 µs that $f_p \sim \nu_{e-Heavy}$. The existence of such temporary conditions of both high attenuation (i.e. high $\nu_{e-Heavy}$) and high electron density (i.e. high f_p) during the interval 50 µs < t < 70 µs facilitates a large power coupling. This dynamic is consistent with a localised attenuation of the axial surface wave power (primarily via the electron-heavy collisions [75]) for the relatively high electron population, which interplay locally during the thermal instability period. After t

>70 µs, stabilised conditions persist in which the reflected power is significantly higher, while the surface wave elongates beyond its expanse at t < 50 µs.

The calculated dielectric properties of the discharge are presented in **Figure 2** e) and f), following formulations in [27, 80, 81]. The refractive index (n), skin depth ($\delta_{\mathrm{skin}}\ (cm)$) and the simulated reflection coefficient (R') of the discharge are given as:

$$\epsilon_r = 1 - \frac{f_p^2\left(1+i\frac{\nu_{e-Heavy}}{f}\right)}{f^2+\nu_{e-Heavy}^2} \quad (8)$$

$$n = n_{Re} + n_{Im} = \sqrt{\epsilon_r} \quad (9)$$

$$\delta_{\mathrm{skin}} = \frac{c}{f\, n_{Im}} \quad (10)$$

$$R' = \frac{(n_{Re}-1)^2 + {n_{Im}}^2}{(n_{Re}+1)^2 + {n_{Im}}^2} \quad (11)$$

Here f is the applied MW frequency = 2.45 GHz, f_p the plasma frequency, n_{Re}, n_{Im} the real and imaginary parts of the refractive index, ϵ_r the relative permittivity and c the speed of light in a vacuum (cm/s).

The skin depth dictates the radial distance over which MW energy is absorbed by the discharge [27, 76] and is presented in **Figure 2** e). A drop from 7 to 0.5 cm in δ_{skin} and a corresponding rise in the discharge refractive index n (**Figure 2** f) correspond with a marked increase in the reflected power (coefficient R', also shown in **Figure 2** f), reaching ~ 90 %. This is slightly higher than the measured reflection coefficient (R in **Figure 2** b), reaching ~ 75 %), but the trend is very similar. Note that the calculated values provide an estimate only, given the formulation employed (equation 11) assumes a plane wave incident on a flat surface and also neglects power coupling in the axial elongation of the discharge [27]. However, it is clear that the reflected power increases circa three-fold following the onset of the thermal instability (50 µs < t < 70 µs). This increase in reflected power eventually limits the affects of the thermal-ionisation instability resulting in more steady discharge conditions (t > 70 µs).

The surface wave propagation is known to occur for the continuously powered state of this discharge and indeed we found that the discharge will eventually settle to a surface wave sustained mode as the lateral plasma elongates. During the initial 'ignition phase' (t < 100 µs) the plasma behaviour does not yet represent characteristics of a surface wave sustained mode. For t > 100 µs, however, our results are conducive with the plasma radius coinciding with the skin depth, marking the onset to a surface sustained mode.

A prominent explanation of ionisation overheating may be that an instability arises due to the exponential dependence of the ionisation rate on the reduced electric field [28, 30, 55, 82]. The logic follows that an increase in the gas temperature results in a decrease in the gas density (N) (under isobaric conditions). This causes an increase in the reduced electric field E/N and the associated electron temperature (T_e), which propagates a feedback loop, causing further ionisation and gas heating. In our case, however, the reduced electric field and T_e (shown in **Figure 2** d) are lower after the thermal

instability onset with the reflected power significantly higher. This nuianced behaviour in the context of pulsed MW discharges motivates a detailed chemical analysis of the discharge.

3.2 Species densities

In **Figure 3** a-d) we present the calculated charged and neutral species densities throughout the power pulse, as obtained from our simulations. In **Appendix 1** the dominant chemical pathways are summarised in terms of production and loss contributions (%) for the key species averaged over the two intervals (0-100 μs & 100-200 μs) of the applied power pulse period.

The charged species densities throughout the pulse are shown in **Figure 3** a). The electron density at t < 50 μs is maintained at $n_e \sim 10^{12}\ cm^{-3}$ but sees a large increase to $n_e \sim 5x10^{13} - 1x10^{14}\ cm^{-3}$ for t > 50 μs during and after the thermal instability onset. The ion density reflects a changing dominance between two main species: N_2^+ and N^+. Until t ~100 μs, N_2^+ dominants as the main ion. In **table 2** a) **Appendix 1**, we see the breakdown of the main N_2^+ production and loss channels. The main production channels reveal that N(^{2}P) associative ionisation [64, 65] (**Figure 3** d) is the key source of N_2^+ which are lost primarily via dissociative ion recombination forming atomic nitrogen species. For t > 70 μs, N^+ begins to dominate with increasing availability of atomic nitrogen in the gas mixture. Indeed, this is consistent with the growing populations of atomic species during this period of the pulse (**Figure 3** b, d). Average production (especially in the 100-200 μs interval) shows sustainment pimarily via charge exchange with N_2^+. Wall losses are not found to represent a significant pathway for ion loss with the exception of N^+ in the first 100 μs with average loss of 11 % found.

The metastable densities for $N_2(a^1\Sigma_u^-)$ and $N_2(A^3\Sigma_u^+)$ along with other prominent electronically species $N_2(B^3\Pi_g)$ and $N_2(C^1\Pi_g)$ are shown in **Figure 3** b). These species are found to be key channels for both electron energy losses (see **section 3.4**) and gas heating (see **section 3.3**) [37, 39, 40]. $N_2(A^3\Sigma)$ is initially the most prominent metastable molecule for t < 50 μs, while both $N_2(A^3\Sigma)$ and $N_2(B^3\Pi)$ are prominent in the remainder of the pulse. Analysis of their production and destruction channels (see **table 2** b) in **Appendix 1**) displays a strong 'population exchange' between $N_2(A^3\Sigma)$ and $N_2(B^3\Pi)$ [39]. This is facilitated by N_2 exchange reactions ($N_2(B^3\Pi) + N_2 \rightarrow N_2(A^3\Sigma) + N_2$ & $N_2(C^3\Pi) + N_2 \rightarrow N_2(B^3\Pi) + N_2$) and pooling reactions of these electronically excited molecular species (i.e. $N_2(A^3\Sigma) + N_2(A^3\Sigma) \rightarrow \Delta H + N_2(v=8) + N_2(B^3\Pi)$, $N_2(A^3\Sigma) + N_2(A^3\Sigma) \rightarrow \Delta H + N_2(v=2) + N_2(C^3\Pi)$ and $N_2(B^3\Pi) + N_2(B^3\Pi) \rightarrow \Delta H + N_2(v=9) + N_2(B^3\Pi)$). Indeed, this tight coupling of the production and loss channels between the metastable and electronically excited molecules somewhat masks the fact that electron impacted $N_2(v)$ (see **section 3.4**) is the key source of metastable production during the pulse.

The density of vibrational levels $N_2(v)$, along with the ground state N_2 density is shown in **Figure 3** c). During the thermal instability, a large drop (up to two orders of magnitude) in the N_2 density occurs to maintain the isobaric conditions as the gas temperature climbs (see **section 3.3**). A large fraction of the neutral gas (i.e. $N_2(v)$=0-43) becomes vibrationally excited during this phase providing a key energy pathway for electronic excitation and ionisation. At t ~ 50 μs, $N_2(v=1)$ is found to make up 21 % of the

N_2(v=0-43) neutral species, while at t ~ 150 μs, it makes up 14 % of the N_2(v=0-43) mix. For higher vibrational levels the excitation peaks show a similar trend. This is illustrated in **Figure 3** c for N_2(v=5) and N_2(v=15), but the other vibrational levels show similar behaviour. At t ~ 50 μs, N_2(v=5) contributes for 5 % of the N_2(v=0-43) neutral species, while at t ~ 150 μs, it makes up 4 % of the N_2(v=0-43) mix. At t ~ 50 μs, N_2(v=15) makes up 0.001 % of the N_2(v=0-43) neutral species while at t ~ 150 μs, it contributes for 0.03 %.

The atomic nitrogen species densities are shown in **Figure 3** d), along with the N_2 conversion (i.e. dissociation to atomic nitrogen) in **Figure 3** e) and the specific energy input (SEI) in **Figure 3** f). Up to t ~ 50 μs, N_2 conversion (shown in **Figure 3** e) remains low (< 0.3 %). Ground state atomic N(^{4}S) shown in **Figure 3** d) dominates the atomic nitrogen population during this period. After the thermal instability onset (t > 50 μs), the N_2 conversion rate increases quickly with a conversion of ~2%, and by t~70 μs, the conversion of N_2 is ~10 % with values saturating near 15 % at t~100 μs. For 70 μs < t < 150 μs N(^{2}D) becomes the dominant excited atomic nitrogen species. In **table 2** c) **Appendix 1** we see this is primarily due to electron impacted excitation from N(^{4}S). Later in the pulse at (t > 150 μs) N(^{2}D) undergoes quenching as the gas temperature rises (see **section 3.4)** with N(^{4}S) again becoming dominant atomic nitrogen species. In **Appendix 1** the production and destruction analysis shows that N(^{4}S) is strongly coupled to N(^{2}D) and N(^{2}P) populations. To understand the fundamental source for Nitrogen conversion here we must therefore consider pathways for N(^{4}S) production outside exchange reactions with N(^{2}D) and N(^{2}P). Dissociation of electronically excited species (shown in **table 2** c) as the collective species N_2^*) is found to have the most impactful contributiuon here. As discussed above electronic excitation of molecular species is primarily due to electron impacted vibrational species. This provides a direct link between the dominant conversion pathways here and vibrational excitation known to be an efficient means for nitrogen fixation[10]. Further, as shown in **table 2** a) **Appendix 1** N_2^+ is primarily formed via associative ionization of N(^{2}P). N(^{2}P) is formed from direct electron impacted excitation with N(^{4}S) and contributions from collisions of $N_2(A^3\Sigma)$ as shown in **tables 2** b) and c). This showns a strong coupling between vibrationally excited species and ion dynamics via electronically excited. At the end of the pulse (t~200 μs), the conversion of N_2 is calculated as ~15 %. Note for the calculated conversion values given here, we take into account any changes in the (mass) density due to stoichiometric changes in the gas mix, i.e. the so-called expansion 'α' factor [83-85]. The specific energy input (SEI) is shown in **Figure 3** f) along with the absorbed power. We see that during the large increase in N_2 conversion (70 μs < t < 100 μs) the SEI ranges 1-2 eV/molecule (or ~100-200 kJ/mol). It must be noted here that the reactor radius (i.e., r_{tube}) is larger than the plasma radius (i.e., r_{plasma}) given the optical emission shown in **Figure 1** b) above. The simulation here therefore represents a sub-volume of the plug volume which is occupied by the discharge (and hence overall conversion predictions would be lower if averaged over the larger plug volume).

In **Figure 3** e) we also show how the gas velocity increases substantially over the pulse period. This is primarily driven by the strong gas heating and subsequent changes to the (mass) density. This, of course, has some limiting effect on the residence time and thus on the overall conversion.

The chemical dynamics of the fast heating and plasma volume contraction will be explained in **section 3.4**. However, in the next section we present the temporal behaviour of the gas and vibrational temperatures, to clearly demonstrate fast heating and its correlation with the plasma volume contraction.

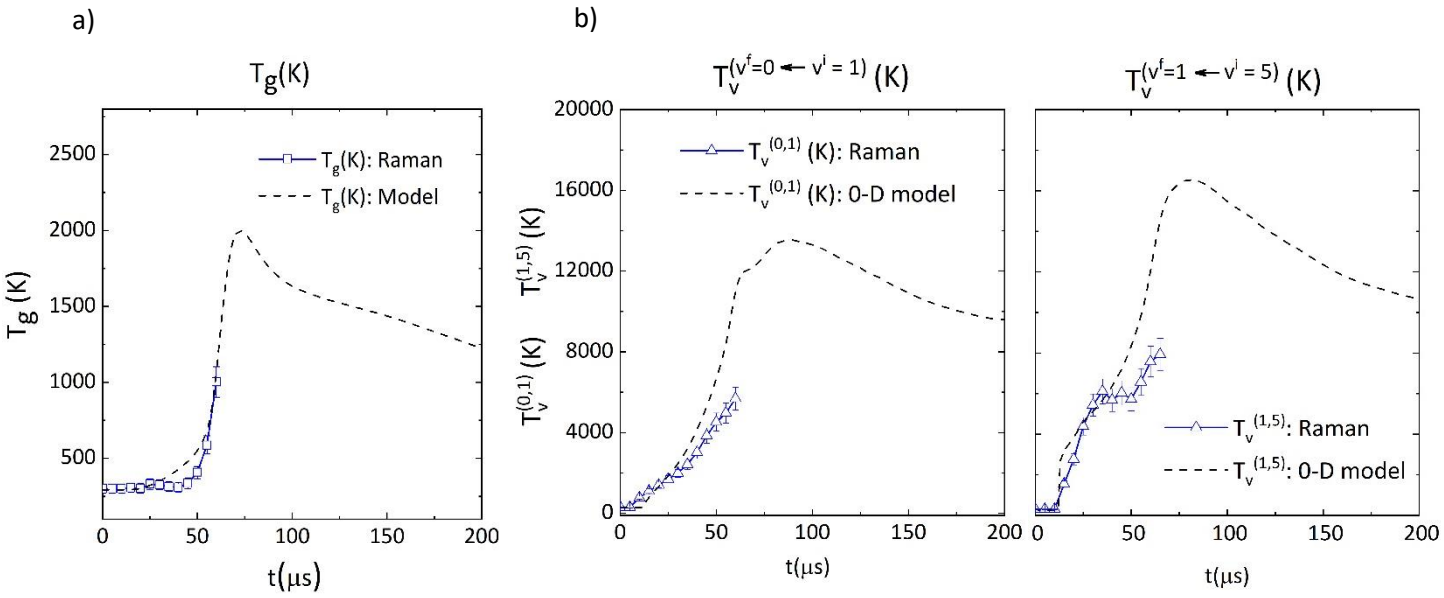

Figure 4: *Comparison of experimental and calculated (**a)** gas temperature T_{gas} (K), and (**b)** vibrational temperature $T_v^{(0,1)}$ (K) and $T_v^{(1,5)}$ (K) (see section 3.3). The accompanying experimental data are the spatially averaged laser scattered Raman measurements.*

3.3 Gas and vibrational temperature

Vibrational Raman spectroscopy (see **section 2.1**) was employed to capture the translational and vibrational gas temperatures across the radial extent of the discharge. The laser was positioned at the central axial position (i.e. x= 0) as shown in **Figure 1** a). In order to compare directly with the 0D simulated translational and vibrational temperatures (**section 2.2**), a radial spatial average of the experimental data is taken.

In **Figure 4** a) we compare the measured spatially-averaged gas temperature (we assume here that the rotational temperature is in equilibrium with the translational gas temperature[21]) and the calculated value. The measured and calculated data show temporal agreement over the range in which experimental data are available. We emphasise the value of modelling here, which enables discovery of trends beyond this time, information which is not available experimentally. Notably, at t ~ 50 μs the translational gas heating rate begins to increase rapidly. This acceleration coincides with the sharp contraction in the discharge volume and the corresponding increase in the power density (see **Figure 2** b). Raman scattering profiles could only be obtained up to t ~ 70 μs, because after t ~ 70 μs the signal-

to-noise ratio prevented further utilisation of the signal. The calculated data, however, allows us to discover the gas temperature beyond this point. In **Figure 4** a) we see an increasing temperature (t > 50 µs) until a peak at t ~ 70 µs of ~2000 K before a gradual decrease to ~1200 K at t ~ 200 µs. Asserting a parabolic temperature profile for the radial changes in the gas temperature we would predict central temperatures given by T_c [K] = 2*T_g – T_w [21]. Assuming a wall temperature 300 K (say) this would give an estimate of T_c~2100 K in the centre of the filament at the end of the pulse period. Unfortunately, it is beyond the scope of the current study to capture detailed gradients and the resulting changes in gas density. However, we believe effectively capturing the average conditions across the filament can give insight into the dominant chemical mechanism involved in the contraction phenomena and in particular the impact of the electronically and vibrationally excited species chemistry on the (spatially averaged) heating rate corroborated experimentally. The focus of this paper is to investigate the chemical aspects of contraction and thermal-ionization phenomena rather than close accuracy. We believe; however, the similar heating rates provide corroboration that support the nature of the trends discovered.

temperatures are shown for vibrational levels v=0,1 and v=1,5, in comparison to the calculated data. The vibrational temperatures T_i are estimated using simulated data based on the ratio of the j^{th} vibrational level to the i^{th} ($j > i$) of the Boltzmann factor [86] between neighbouring vibrational number densities $n_{i,j}$ and the associated vibrational energy levels ($E_{i,j}$) of N_2 as:

$$T_v^{(v=i\leftarrow v=j)} = -\frac{E_j - E_i}{\ln\left(\frac{n_j}{n_i}\right)} \qquad (11)$$

Here the vibrational temperature for $T_v^{(v=i\leftarrow v=j)}$ is estimated for vibrational levels from v=1,…,5.

The vibrational temperatures $T_v^{(v=0\leftarrow v=1)}$ and $T_v^{(v=1\leftarrow v=5)}$ (**Figure 4** b) show a steady heating rate for t < 50 µs with temperatures significantly exceeding the translational gas temperature T_g. After t ~ 50 µs, the vibrational temperatures (**Figure 4** b) rise abruptly due to the thermal instability onset. The ratio of $T_{v=1}/T_g$ (an indicator of the extent of thermal non-equilibrium between the translational and vibrational temperatures [21]) is found to be 7 at t ~ 30 µs, rising to 12 at t ~ 50 µs, and to 8 at t ~ 100 µs. This constitutes a significant non-equilibrium between the gas (translational) and vibrational temperatures. For $T_{v=5}/T_g$ we see (**Figure 4**) a larger non-equilibrium. $T_{v=5}/T_g$ is 13 at t ~ 30 µs, 15 at t ~ 50 µs, and 9 at t ~ 100 µs. $T_{v=15}/T_g$ shows similar behaviour to $T_{v=5}/T_g$ consistent with $T_{v>1}$ reaching a quasi-equilibrium later in the pulse (see **Figure 4**).

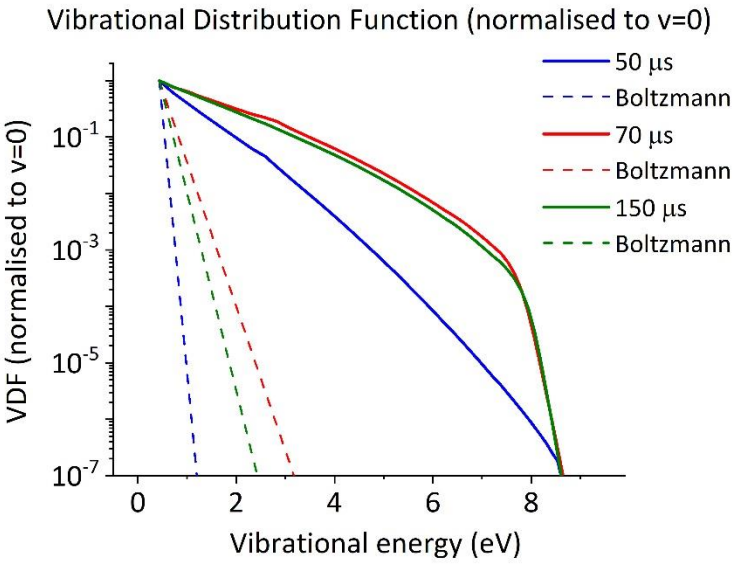

***Figure 5**: Calculated vibrational distribution function normalised to density of N_2(v=0) at different times during pulse period.*

In **Figure 5** we plot the calculated vibrational distribution function (VDF) (normalised to v=0) at various prominent times throughout the discharge pulse, along with the corresponding Boltzmann distribution, which represents the equivalent equilibrium vibrational distribution at that particular gas temperature. At t ~ 50 µs, the upper vibrational levels have become strongly heated with a significant non-equilibrium compared to the Boltzmann distribution. $T_v^{(0,1)}$ and $T_v^{(1,5)}$ (**Figure 4** b) lie close to the electron temperature of ~1.25 eV (~14,500 K) at t ~ 150-200 µs; see **Figure 2** d). This behaviour is also seen clearly in the VDF shown in **Figure 5**. Indeed at t ~ 150 µs the VDF is still significantly overpopulated compared to its equivalent Boltzmann distribution at this gas temperature (T_g ~ 1,200 K).

The downwards bend in the VDF tail for vibrational energies > 6 eV observed at t ≥70 µs (see **Figure 5**) coincides with the excitation energies of the key electronic states (e.g. $N_2(A^3\Sigma)$ = 6.2 eV, $N_2(B^3\prod)$ = 7.4eV). This is consistent with electron impact excitation of $N_2(v)$ as a dominant production pathway. The consequent role of the metastables in the fast gas heating and plasma volume contraction will be explained in the next section.

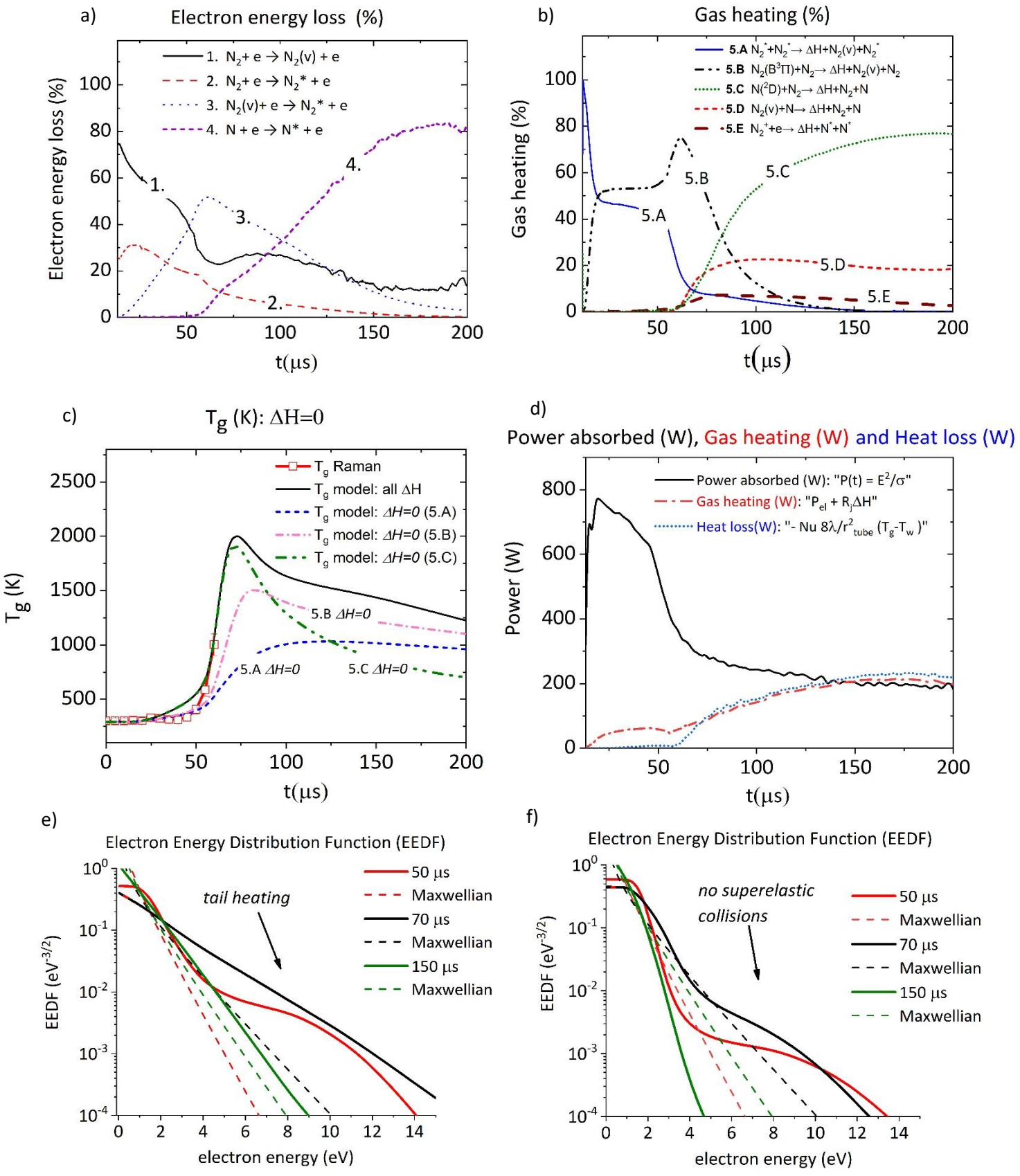

Figure 6: a) *Electron energy transfer into various electron impact reactions during pulse.* ***b)*** *% contribution of various processes to gas heating.* ***c)*** *gas heating contributions turned off (⊿H=0) for key reactions.* ***d)*** *Power absorbed from external power (W), gas heating (W) and heat loss to walls (last term on rhs of equation 5).* ***e)*** *Electron energy distribution function ($eV^{-3/2}$) at different times during pulse, along with the equivalent Maxwellian EEDF.* ***f)*** *equivalent EEDF with superelastic collisions removed.*

Reaction type	Characteristic reaction	Characteristic time (μs)
1. e-vib	N_2+ e → N_2(v=1) + e	2
2. e-meta	N_2+ e → $N_2(B^3\Pi)$ + e	69
3. e-vib-meta	N_2(v=1)+ e → $N_2(B^3\Pi)$ + e	61
4. e-N-excit	N + e → $N(^2D)$ + e	4
5 A. Pooling	$N_2(A^3\Sigma)$+$N_2(A^3\Sigma)$ → ΔH + N_2(v=8) + $N_2(B^3\Pi)$	4
	$N_2(A^3\Sigma)$ + $N_2(A^3\Sigma)$ → ΔH +N_2(v=2) + $N_2(C^3\Pi)$	2
	$N_2(B^3\Pi)$ + $N_2(B^3\Pi)$ →ΔH+ N_2(v=9) + $N_2(B^3\Pi)$	4
5 B. $N_2(B^3\Pi)$-N_2	$N_2(B^3\Pi)$ + N_2 → ΔH + N_2 + N_2	0.8
5 C. $N(^2D)$-N	$N(^2D)$ + N_2 → ΔH + N_2 + N(4S)	17
5 D. VT-N	N_2(v=7) + $N(^4S)$ → ΔH + N_2(v=6) + $N(^4S)$	820
5 E. $N(^2D)$-N	$N(^2D)$ + N_2 → ΔH + N_2 + $N(^4S)$	17

Table 1**: Characteristic reactions and characteristic time (μs) of the main (representative) reactions for electron energy loss (1-4) and gas heating (5.A-E). See **Figure 6.

3.4 Electron energy distribution and underlying reasons for fast gas heating

The energy flow in the chemical system begins with an externally applied electric field, heating electrons (facilitated by their relatively small mass compared to the ions). Heated electrons then transfer energy via a myriad of collisions (over a variety of timescales) with heavy gas species. In **Figure 6** a) we present a temporal sequence of the fractional loss of electron energy [4, 39] for the three dominant groups of reactions, namely, 1: electron impact vibrational excitation (v=1-43), 2: electronic excitation of N_2 to the metastable (and other electronically excited) levels (where N_2* represents the $N_2(A^1\Sigma)$, $N_2(A^3\Sigma)$, $N_2(B^3\Pi)$ and $N_2(C^1\Pi)$ electronically excited states), 3: electronic excitation of vibrational levels to an electronically excited metastable and 4. Excitation of atomic N to $N(^2P)$ and $N(^2D)$ excited states. For 0 < t < 50 μs (before the onset of the thermal instability) electron impact vibrational excitation dominates (~60-70 %), while electronic excitation of the ground state to the metastable levels makes up a minority share of electron energy loss (~15-20 %). At t ~ 50 μs (during the thermal instability onset) electron energy loss is quickly redirected to electronic excitation of metastable species from vibrationally excited species. Later in the pulse, after some stabilisation (t > 70 μs), the electron energy goes to substaintially towards excitation of atomic nitrogen species as their populations grow in the gas mixture.

In **table 1** we list the characteristic times associated with the collisional processes presented in **Figure 6**. For each group of reactions, we have chosen a representative reaction [21]. The characteristic time is achieved by integration of the reaction rates associated with each grouping over the 200 μs pulse period. Correlation of **table 1** with the electron energy loss fractions in **Figure 6** a) offers an insight into the timescales of the dominant chemical pathways. Electron impact vibrational excitation with a

characteristic time of ~2 μs dominates in the early stages of the pulse. In comparison, electron impact excitation to the metastable levels from the ground state or vibrational levels exhibits a characteristic time of 69 and 61 μs, respectively, corresponding with the onset of the thermal instability.

In **Figure 6** b) the relative contributions to gas heating are shown over the pulse period (with the corresponding characteristic reactions and times shown in **table 1)**. The corresponding absolute values for gas heating power are further shown in **Figure 6** d) along with wall heat loss and the total power absorbed. **Figure 6** b) shows that quenching of electronically excited molecular species dominate in gas heating from the very beginning up to 70 μ. This includes self-quenching via Pooling reactions (i.e.: $N_2(A^3\Sigma) + N_2(A^3\Sigma) \rightarrow \Delta H + N_2(v=8) + N_2(B^3\Pi)$, $N_2(A^3\Sigma) + N_2(A^3\Sigma) \rightarrow \Delta H + N_2(v=2) + N_2(C^3\Pi)$) and) and $N_2(B^3\Pi) + N_2(B^3\Pi) \rightarrow \Delta H + N_2(v=9) + N_2(B^3\Pi)$ and direct quenching of $N_2(B^3\Pi)$ with N_2. Clearly, this is key part of the instigation of the fast gas heating rate and corresponding discharge volume contraction observed. The characteristic time for the three pooling reactions is estimated at 2-4 μs and the $N_2(B^3\Pi)$ with N_2 quenching at 4 μs consistent with the quick acceleration of the gas temperature observed experimentally. In the later stages of the pulse (t~100 μs), the contributions associated with formation of atomic nitrogen species become important gas heating pathways. Quenching of $N(^2D)$ to $N(^4S)$ is especially important along with smaller contributions from 'VT-N' (vibrational-translation interaction of $N_2(v)$ with N).

In **Figure 6** c) we see the impact of various quenching reactions of electronically excited molecular or atomic species on the calculated gas temperature with enthalpy contributions 'turned off' for key heating reactions. In the first half of the discharge (up to t ~100 μs) the various Pooling reactions (5.A) have the most significant impact on the heating rate, but with important contributions also from $N_2(B^3\Pi)$ quenching (5.B). In the second half of the pulse (t > 100 μs) quenching of $N(^2D)$ to $N(^4S)$ becomes a primary pathway for gas heating as atomic nitrogen species grow in population within the gas mixture.

In **Figure 6** e) the electron energy distribution function (EEDF) is presented at t ~ 50, 70 and 150 μs, along with the equivalent Boltzmann distribution at the corresponding electron energy (ε) (see **Figure 2 d**). Indeed, by t ~ 50 μs a large deviation in the EEDF tail is already found. Beyond t > 50 μs, this 'tail heating' persists, eventually leading to a large growth in metastable densities, causing a high gas heating rate at t > 50 μs, due to the 'pooling reactions'. Tail heating is due to energy exchange with vibrationally excited $N_2(v)$ molecules (i.e. super-elastic collisions). Strong heating, especially for ε > 5 eV (which is near the threshold for excitation of metastable species) is seminal for providing a population of heated electrons, which precipitate the dynamic chemistry in the discharge. The delayed transition of the EEDF to a Maxwellian discharge in the latter stages of the pulse at t ~ 150 μs (see **Figure 6** e)) where the ionisation fraction remains high may be due to the relative drop in absorbed power. The instigation of the thermal-ionization contraction results in a large increase in reflected power on timescales not controllable for the manual impedance tuner hence the absorbed power falls significantly in the latter stage of the pulse. In **Figure 6** f) the electron energy distribution function (EEDF) is presented at t ~ 50, 70 and 150 μs, along with the equivalent Boltzmann distribution at the corresponding electron energy (ε) without the inclusion of superelastic collisions between electron and both vibrationally and electronically excited species. By comparing with **Figure 6** e), we can see that the extent of the tail heating is significantly suppressed, corroborating the discussions above about the important role of superelastic collisions in tail heating of the EEDF.

In summary, tail heating of the EEDF offers a fundamental explanation of how the thermal-ionisation instability is instigated in the presence of high vibrational excitation, with an overall decreasing reduced electric field [34], contrary to conventional explanations of thermal ionisation instabilities dominated by direct electron impact ionisation processes [55]. The changing dynamics of the plasma dielectric properties and in particular the large increase in reflected power (see **section 3.1**) eventually provides a stabilising affect to the super-elastic driven thermal-ionisation instability. It must, however, be recognised that a clear description of why the discharge contraction occurs remains unanswered, and only a model that computes the spacial dynamics may give a satisfactory answer. It is indeed a very hard quest, because the discharge transits from a spherical to cylindrical symmetry while the electric field accommodates to the time varying plasma (in volume and parameters).

4. Conclusions

A key challenge in applications involving pulse-powered plasma gas conversion technologies lies in a greater understanding of plasma dynamics. Illucidating the nature of thermal-ionisation instabilities in molecular MW plasmas (in this case N_2) is central to addressing scalability and intensification challenges for plasma conversion applications, particularly under pulsed conditions where ignition is frequent. In this report, we studied the dynamics of an isolated power pulse ignited in a vortex flow stabilised MW plasma in N_2 at sub-atmospheric pressure (25 mbar), by a combination of a 0D kinetics model, iCCD imaging and laser scattering diagnostics.

Quenching of $N_2(A^3\Sigma)$ and $N_2(B^3\prod)$ electronically excited molecules is found to result in fast gas heating, which induces a thermal-ionisation instability. This results in a discharge volume contraction leading to significant changes in the discharge dielectric properties (**section 3.1**), species densities (**section 3.2**), gas and vibrational temperatures (**section 3.3**) and the distribution of energy within the chemical system (**section 3.4**).

The onset of a thermal-ionisation instability (t > 50 μs), causes the N_2 conversion rate to increase significantly. The changing ratio of f_p and $\nu_{e-Heavy}$ results in fundamentally different dielectric properties for the discharge before/after the thermal instability which manifests as a significant increase in the reflected power after the thermal instability onset. As the dielectric properties of the discharge change during the instability, a higher power density is briefly coupled to the discharge before this is limited by an increased reflected power. The instability onset enhances the relative electron population, while the collision frequency lowers as the temperature rises and gas density drops to maintain isobaric conditions. A significant increase in the power reflected by the plasma eventually stabilises the discharge with power density levels lowering to pre-instability levels. Translational and vibrational gas temperature analysis reveals a quasi-non-equilibrium is reached within the pulse after the discharge contraction, with the translational temperature stabilising at ~1200 K, while vibrational temperatures are found in near equilibrium with the electron energy (~1 eV).

Radial contraction of the discharge to the skin depth is found to occur after the contraction phase (t~100 μs), while the surface wave induced axial elongation is found to be temporarily contracted during the thermal instability onset. The reduced electric field is found to increase only slightly during the

thermal instability before decreasing significantly compared to levels before the thermal instability onset. The (average) electron temperature shows a similar trend. This is contrary to the thermal-ionisation mechanism reported for other gas mixtures and reactors, which are likely less vibrationally activated and not prone to the dynamic power absorbed conditions of MW discharge. The chemistry is shown here to be fundamentally driven by electron impact N_2 vibrational excitation and super-elastic heating of the electron energy distribution tail, causing strong electronic excitation from the vibrational levels towards the metastable levels, which then instigate fast gas heating by the quenching of electronically excited species. Ionisation dynmaics are also found here to be fundamentally driven by vibrational excitation. This dynamic reveals how the thermal-ionisation instability can occur in the presence of high vibrational excitation in a MW discharge during the initial moments of ignition for a continuously power discharge or in the breakdown during an applied power pulse. This research is crucial for progressing a fundamental basis for N_2 fixation using pulsed-power MW technology, informing key industrial challenges, such as process intensification and scalability.

Acknowledgements

SK & AB acknowledge financial support by the European Marie Skłodowska-Curie Individual Fellowship "PENFIX" within Horizon 2020 (Grant No. 838181), the European Research Council (ERC) under the European Union's Horizon 2020 research and innovation programme (grant agreement No 810182 – SCOPE ERC Synergy project), and the Excellence of Science FWO-FNRS project (FWO grant ID GoF9618n, EOS ID 30505023). The calculations were performed using the Turing HPC infrastructure at the CalcUA core facility of the Universiteit Antwerpen (UAntwerpen), a division of the Flemish Supercomputer Centre VSC, funded by the Hercules Foundation, the Flemish Government (department EWI) and the UAntwerpen. SK and AB would like to thank Mr. Luc van 't dack, Dr. Karen Leyssens and Ing. Karel Venken for their technical assistance. AvdS, AH and GvR are grateful to Ampleon for the use of their solid-state microwave amplifier units and acknowledge financial support from the Netherlands Organisation for Scientific Research (NWO grant number 733.000.002) in the framework of the CO_2-to-Products program with kind support from Shell, and the ENW PPP Fund for the top sectors. This project has been partially funded by the European Union's Horizon 2020 research and innovation programme 'Pioneer' under the Marie Skłodowska-Curie grant agreement No 813393.

Appendix 1

Production			
Species	**Reaction**	**0-100 µs** **%**	**100-200 µs** **%**
N_2^+	$N(^2P) + N(^2P) \rightarrow N_2^+ + \mathbf{e}$	97	94
N^+	$N_2^+ + N(^4S) \rightarrow N^+ + N_2$	92	99
	$N(^4S) + \mathbf{e} \rightarrow e + N^+$	8	-

Destruction			
Species	**Reaction**	**0-100 µs** **%**	**100-200 µs** **%**
N_2^+	$N_2^+ + \mathbf{e} \rightarrow \Delta H + N(^4S) + N(^4S)$	42	44
	$N_2^+ + \mathbf{e} \rightarrow \Delta H + N(^4S) + N(^2D)$	42	44
N^+	$N^+ + N(^4S) + N_2 \rightarrow N_2^+ + N_2$	77	88
	$N^+ \rightarrow$ wall	11	2

Table 2 a)*: Reaction analysis over the pulse period: % contributions from dominant production and loss channels for key ionic species. Reaction groupings with negigible contributions which are not impactful have typically been excluded/ filtered out in the above table to show the dominant chemical pathways.*

Production			
Species	**Reaction**	**0-100 µs %**	**100-200 µs %**
$N_2(A^3\Sigma)$	$N_2(B^3\prod) + N_2 \rightarrow N_2(A^3\Sigma) + N_2$	52	38
	$N_2(v) + e \rightarrow N_2(A^3\Sigma) + e$	44	58
	$N_2 + e \rightarrow N_2(A^3\Sigma) + e$	4	3
$N_2(B^3\prod)$	$N_2(v) + e \rightarrow N_2(B^3\prod) + e$	50	82
	$N_2(C^3\prod) + N_2 \rightarrow N_2(B^3\prod) + N_2$	33	6
	$N_2(A^3\Sigma) + N_2(A^3\Sigma) \rightarrow \Delta H + N_2(v=8) + N_2(B^3\prod)$	12	2

Destruction			
Species	**Reaction**	**0-100 µs %**	**100-200 µs %**
$N_2(A^3\Sigma)$	$N_2(A^3\Sigma) + N_2(A^3\Sigma) \rightarrow \Delta H + N_2(v=8) + N_2(B^3\prod)$	21	3
	$N_2(A^3\Sigma) + N_2(A^3\Sigma) \rightarrow \Delta H + N_2(v=2) + N_2(C^3\prod)$	41	1
	$N_2(A^3\Sigma) + e \rightarrow N_2 + e$	23	12
	$N_2(A^3\Sigma) + N(^4S) \rightarrow N_2 + N(^2P)$	11	75
	$N_2(A^3\Sigma) + N(^4S) \rightarrow N_2 + N(^4S)$	2	10
$N_2(B^3\prod)$	$N_2(B^3\prod) + N_2 \rightarrow N_2(A^3\Sigma) + N_2$	55	82
	$N_2(B^3\prod) + e \rightarrow N_2 + e$	38	13
	$N_2(B^3\prod) + N_2(B^3\prod) \rightarrow \Delta H + N_2(B^3\prod) + N_2(v=9)$	5	-
	$N_2(B^3\prod) + N_2 \rightarrow \Delta H + N_2 + N_2$	3	5

Table 2 b)*: Reaction analysis over the pulse period: % contributions from dominant production and loss channels for key metastable and electronically excited molecular species. Contributions from reactions with two and three bodies have been combined. Reaction groupings with negigible contributions which are not impactful have typically been excluded/ filtered out in the above table to show the dominant chemical pathways.*

Production			
Species	**Reaction**	**0-100 µs %**	**100-200 µs %**
$N(^4S)$	$N_2(v) + e \rightarrow N(^4S) + N(^4S) + e$	18	-
	$N_2^* + e \rightarrow \Delta H + N(^4S) + N(^4S)$	17	-
	$N(^2D) + N_2 \rightarrow \Delta H + N(^4S) + N_2$	40	98
$N(^2D)$	$N(^4S) + e \rightarrow N(^2D) + e$	82	87
	$N(^2P) + N(^4S) \rightarrow N(^4S) + N(^2D)$	3	7
	$N_2^+ + e \rightarrow \Delta H + N(^2D) + N(^2D)$	10	4
$N(^2P)$	$N(^4S) + e \rightarrow N(^2P) + e$	57	72
	$N_2(A^3\Sigma) + N(^4S) \rightarrow N_2 + N(^2P)$	40	26

Destruction			
Species	**Reaction**	**0-100 µs %**	**100-200 µs %**
$N(^4S)$	$N(^4S) + e \rightarrow e + N(^2D)$	71	87
	$N(^4S) + e \rightarrow e + N(^2P)$	15	9
	$N_2(A^3\Sigma) + N(^2P) \rightarrow N_2 + N(^4S)$	14	3
$N(^2D)$	$N(^2D) + N_2 \rightarrow \Delta H + N(^4S) + N_2$	99	99
$N(^2P)$	$N(^2P) + N(^2P) \rightarrow N_2^+ + \mathbf{e}$	91	53
	$N(^2P) + N(^4S) \rightarrow N(^2D) + N(^4S)$	9	47

Table 2 c)*: Reaction analysis over the pulse period: % contributions from dominant production and loss channels for atomic nitrogen species. Contributions from reactions with two and three bodies have been combined. Contributions from $N_2(v)$ vibrational levels have been summed. The term N_2^* represents the collection of metastable and electronically excited molecular species (see* ***table 2*** *b). Reaction groupings with negigible contributions which are not impactful have typically been excluded/ filtered out in the above table to show the dominant chemical pathways.*

References

[1] S. Pancheshnyi, B. Eismann, G.J.M. Hagelaar, L.C. Pitchford, Computer code ZDPlasKin, University of Toulouse, LAPLACE, CNRS-UPS-INP, Toulouse, France., DOI www.zdplaskin.laplace.univ-tlse.fr (2008).
[2] G.D.B.a.S. Thompson, DVODE solver - ordinary differential equation (ode) solver - a Fortran 90 version of the well-known VODE ode solver by Brown, Byrne, and Hindmarsh, http://www.radford.edu/thompson/vodef90web.html, 2013.
[3] G.J.M. Hagelaar, L.C. Pitchford, Solving the Boltzmann equation to obtain electron transport coefficients and rate coefficients for fluid models, Plasma Sources Science and Technology, 14 (2005) 722-733.
[4] A. Bogaerts, E.C. Neyts, Plasma Technology: An Emerging Technology for Energy Storage, ACS Energy Letters, 3 (2018) 1013-1027.
[5] IRENA, Global energy transformation: A roadmap to 2050 (2019 edition), International Renewable ENergy Agency (IRENA), DOI https://www.irena.org(2019).
[6] B.S. Patil, Q. Wang, V. Hessel, J. Lang, Plasma N2-fixation: 1900–2014, Catalysis Today, 256 (2015) 49-66.
[7] H. Patel, R.K. Sharma, V. Kyriakou, A. Pandiyan, S. Welzel, M.C.M. Van De Sanden, M.N. Tsampas, Plasma-Activated Electrolysis for Cogeneration of Nitric Oxide and Hydrogen from Water and Nitrogen, ACS Energy Letters, DOI 10.1021/acsenergylett.9b01517(2019) 2091-2095.
[8] Y. Gorbanev, E. Vervloessem, A. Nikiforov, A. Bogaerts, Nitrogen Fixation with Water Vapor by Nonequilibrium Plasma: toward Sustainable Ammonia Production, ACS Sustainable Chemistry & Engineering, 8 (2020) 2996-3004.
[9] P. Peng, P. Chen, M. Addy, Y. Cheng, Y. Zhang, E. Anderson, N. Zhou, C. Schiappacasse, R. Hatzenbeller, L. Fan, S. Liu, D. Chen, J. Liu, Y. Liu, R. Ruan, In situ plasma-assisted atmospheric nitrogen fixation using water and spray-type jet plasma, Chemical Communications, 54 (2018) 2886-2889.
[10] W. Wang, B. Patil, S. Heijkers, V. Hessel, A. Bogaerts, Nitrogen Fixation by Gliding Arc Plasma: Better Insight by Chemical Kinetics Modelling, ChemSusChem, 10 (2017) 2145-2157.
[11] R. Brandenburg, A. Bogaerts, W. Bongers, A. Fridman, G. Fridman, B.R. Locke, V. Miller, S. Reuter, M. Schiorlin, T. Verreycken, K.K. Ostrikov, White paper on the future of plasma science in environment, for gas conversion and agriculture, Plasma Processes and Polymers, 16 (2019) 1700238.
[12] K. Van 'T Veer, F. Reniers, A. Bogaerts, Zero-dimensional modeling of unpacked and packed bed dielectric barrier discharges: the role of vibrational kinetics in ammonia synthesis, Plasma Sources Science and Technology, 29 (2020) 045020.
[13] E. Vervloessem, M. Aghaei, F. Jardali, N. Hafezkhiabani, A. Bogaerts, Plasma-Based N2 Fixation into NOx: Insights from Modeling toward Optimum Yields and Energy Costs in a Gliding Arc Plasmatron, ACS Sustainable Chemistry & Engineering, 8 (2020) 9711-9720.
[14] A. Berthelot, A. Bogaerts, Modeling of CO2 Splitting in a Microwave Plasma: How to Improve the Conversion and Energy Efficiency, The Journal of Physical Chemistry C, 121 (2017) 8236-8251.
[15] A. Fridman, Plasma Chemistry, Cambridge University Press, Cambridge, 2008.
[16] R.I. Asisov, Givotov, V. K., Rusanov, V. D., Fridman, A., High Energy Chemistry (Khimia Vysokikh Energij, Sov. Phys., 14 (1980) 366.
[17] W. Bongers, H. Bouwmeester, B. Wolf, F. Peeters, S. Welzel, D. Van Den Bekerom, N. Den Harder, A. Goede, M. Graswinckel, P.W. Groen, J. Kopecki, M. Leins, G. Van Rooij, A. Schulz, M. Walker, R. Van De Sanden, Plasma-driven dissociation of CO2 for fuel synthesis, Plasma Processes and Polymers, 14 (2017) 1600126.
[18] V. Vermeiren, A. Bogaerts, Supersonic Microwave Plasma: Potential and Limitations for Energy-Efficient CO2 Conversion, The Journal of Physical Chemistry C, 122 (2018) 25869-25881.
[19] V.D. Rusanov, A.A. Fridman, The physics of a chemically active plasma, MoIzN, DOI (1984).
[20] M. Baeva, X. Luo, B. Pfelzer, J. Uhlenbusch, Theoretical investigation of pulsed microwave discharge in nitrogen, Plasma Sources Science and Technology, 8 (1999) 404-411.
[21] S. Van Alphen, V. Vermeiren, T. Butterworth, D.C.M. Van Den Bekerom, G.J. Van Rooij, A. Bogaerts, Power Pulsing To Maximize Vibrational Excitation Efficiency in N2 Microwave Plasma: A Combined Experimental and Computational Study, The Journal of Physical Chemistry C, 124 (2020) 1765-1779.
[22] V. Vermeiren, A. Bogaerts, Improving the Energy Efficiency of CO2 Conversion in Nonequilibrium Plasmas through Pulsing, The Journal of Physical Chemistry C, 123 (2019) 17650-17665.
[23] D.C.M. van den Bekerom, J.M.P. Linares, T. Verreycken, E.M. van Veldhuizen, S. Nijdam, G. Berden, W.A. Bongers, M.C.M. van de Sanden, G.J. van Rooij, The importance of thermal dissociation in CO2 microwave discharges investigated by power pulsing and rotational Raman scattering, Plasma Sources Science and Technology, 28 (2019) 055015.
[24] E. Carbone, S. Nijdam, Ultra-fast pulsed microwave plasma breakdown: evidence of various ignition modes, Plasma Sources Science and Technology, 23 (2013) 012001.
[25] S.N. Andreev, V.V. Zakharov, V.N. Ochkin, S.Y. Savinov, Plasma-chemical CO2 decomposition in a non-self-sustained discharge with a controlled electronic component of plasma, Spectrochimica Acta Part A: Molecular and Biomolecular Spectroscopy, 60 (2004) 3361-3369.

[26] I. Belov, V. Vermeiren, S. Paulussen, A. Bogaerts, Carbon dioxide dissociation in a microwave plasma reactor operating in a wide pressure range and different gas inlet configurations, Journal of CO2 Utilization, 24 (2018) 386-397.
[27] N. Den Harder, D.C.M. Van Den Bekerom, R.S. Al, M.F. Graswinckel, J.M. Palomares, F.J.J. Peeters, S. Ponduri, T. Minea, W.A. Bongers, M.C.M. Van De Sanden, G.J. Van Rooij, Homogeneous CO2conversion by microwave plasma: Wave propagation and diagnostics, Plasma Processes and Polymers, 14 (2017) 1600120.
[28] A.J. Wolf, T.W.H. Righart, F.J.J. Peeters, W.A. Bongers, M.C.M. Van De Sanden, Implications of thermo-chemical instability on the contracted modes in CO2 microwave plasmas, Plasma Sources Science and Technology, 29 (2020) 025005.
[29] A.J. Wolf, T.W.H. Righart, F.J.J. Peeters, P.W.C. Groen, M.C.M. Van De Sanden, W.A. Bongers, Characterization of CO2 microwave plasma based on the phenomenon of skin-depth-limited contraction, Plasma Sources Science and Technology, 28 (2019) 115022.
[30] Y. Kabouzi, M.D. Calzada, M. Moisan, K.C. Tran, C. Trassy, Radial contraction of microwave-sustained plasma columns at atmospheric pressure, Journal of Applied Physics, 91 (2002) 1008-1019.
[31] M.A. Ridenti, J. De Amorim, A. Dal Pino, V. Guerra, G. Petrov, Causes of plasma column contraction in surface-wave-driven discharges in argon at atmospheric pressure, Physical Review E, 97 (2018).
[32] A. Fridman, L.A. Kennedy, Plasma Physics and Engineering, Taylor & Francis2004.
[33] M. Baeva, X. Luo, B. Pfelzer, J.H. Schäfer, J. Uhlenbusch, Z. Zhang, Experimental study of pulsed microwave discharges in nitrogen, Plasma Sources Science and Technology, 8 (1999) 142-150.
[34] E. Tatarova, F.M. Dias, C.M. Ferreira, V. Guerra, J. Loureiro, E. Stoykova, I. Ghanashev, I. Zhelyazkov, Self-consistent kinetic model of a surface-wave-sustained discharge in nitrogen, Journal of Physics D: Applied Physics, 30 (1997) 2663-2676.
[35] E. Castaños Martinez, Y. Kabouzi, K. Makasheva, M. Moisan, Modeling of microwave-sustained plasmas at atmospheric pressure with application to discharge contraction, Physical Review E, 70 (2004) 066405.
[36] Y.B. Golubovskii, V. Nekuchaev, S. Gorchakov, D. Uhrlandt, Contraction of the positive column of discharges in noble gases, Plasma Sources Science and Technology, 20 (2011) 053002.
[37] V. Guerra, A. Tejero-Del-Caz, C.D. Pintassilgo, L.L. Alves, Modelling N2–O2 plasmas: volume and surface kinetics, Plasma Sources Science and Technology, 28 (2019) 073001.
[38] N.A. Popov, Fast gas heating in a nitrogen–oxygen discharge plasma: I. Kinetic mechanism, Journal of Physics D: Applied Physics, 44 (2011) 285201.
[39] V. Guerra, P.A. Sá, J. Loureiro, Role played by the N 2 (A 3 Σ u +) metastable in stationary N 2 and N 2 -O 2 discharges, 34 (2001) 1745-1755.
[40] V. Guerra, E. Tatarova, F.M. Dias, C.M. Ferreira, On the self-consistent modeling of a traveling wave sustained nitrogen discharge, 91 (2002) 2648.
[41] N.D. Lepikhin, N.A. Popov, S.M. Starikovskaia, Fast gas heating and radial distribution of active species in nanosecond capillary discharge in pure nitrogen and N2:O2mixtures, Plasma Sources Science and Technology, 27 (2018) 055005.
[42] I. Shkurenkov, I.V. Adamovich, Energy balance in nanosecond pulse discharges in nitrogen and air, Plasma Sources Science and Technology, 25 (2016) 015021.
[43] M.M. Nudnova, S.V. Kindysheva, N.L. Aleksandrov, A.Y. Starikovskii, Fast gas heating in N₂/O₂ mixtures under nanosecond surface dielectric barrier discharge: the effects of gas pressure and composition, Philosophical Transactions of the Royal Society A: Mathematical, Physical and Engineering Sciences, 373 (2015) 20140330.
[44] C.D. Pintassilgo, V. Guerra, Power Transfer to Gas Heating in Pure N2 and in N2–O2 Plasmas, The Journal of Physical Chemistry C, 120 (2016) 21184-21201.
[45] B.F. Gordiets, C.M. Ferreira, V.L. Guerra, J.M.A.H. Loureiro, J. Nahorny, D. Pagnon, M. Touzeau, M. Vialle, Kinetic model of a low-pressure N/sub 2/-O/sub 2/ flowing glow discharge, IEEE Transactions on Plasma Science, 23 (1995) 750-768.
[46] Y. Akishev, M. Grushin, V. Karalnik, A. Petryakov, N. Trushkin, On basic processes sustaining constricted glow discharge in longitudinal N2flow at atmospheric pressure, Journal of Physics D: Applied Physics, 43 (2010) 215202.
[47] M. Capitelli, D. Bruno, A. Laricchiuta, Fundamental aspects of plasma chemical physics, Transport, 74 (2013).
[48] N. Gatti, S. Ponduri, F.J.J. Peeters, D.C.M. Van Den Bekerom, T. Minea, P. Tosi, M.C.M. Van De Sanden, G.J. Van Rooij, Preferential vibrational excitation in microwave nitrogen plasma assessed by Raman scattering, Plasma Sources Science and Technology, 27 (2018) 055006.
[49] D.A. Long, Raman spectroscopy, McGraw-Hill Book Company, New York; St. Louis; San Francisco; [etc.], 1977.
[50] A. Belikov, G. Sukhinin, Nitrogen rotation relaxation time measured in freejets, DOI (1989).
[51] A. Lo, G. Cléon, P. Vervisch, A. Cessou, Spontaneous Raman scattering: a useful tool for investigating the afterglow of nanosecond scale discharges in air, Applied Physics B, 107 (2012) 229-242.
[52] A. Montello, Z. Yin, D. Burnette, I.V. Adamovich, W.R. Lempert, Picosecond CARS measurements of nitrogen vibrational loading and rotational/translational temperature in non-equilibrium discharges, Journal of Physics D: Applied Physics, 46 (2013) 464002.

[53] T.B. A.W. van de Steeg, D.C.M. van den Bekerom, A.F. Sovelas da Silva, M.C.M. van de Sanden, G.J. van Rooij, Greenhouse gas utilization and electrification of nitrogen fixation: can vibrational excitation in the plasma phase offer non-thermal opportunities?, Plasma Sources Science and Technology, Submitted (2020).
[54] C.D. Pintassilgo, V. Guerra, O. Guaitella, A. Rousseau, Study of gas heating mechanisms in millisecond pulsed discharges and afterglows in air at low pressures, Plasma Sources Science and Technology, 23 (2014) 025006.
[55] M. Capitelli, C.M. Ferreira, B.F. Gordiets, A.I. Osipov, Plasma Kinetics in Atmospheric Gases, Springer Berlin Heidelberg2013.
[56] T. Kozák, A. Bogaerts, Evaluation of the energy efficiency of CO2conversion in microwave discharges using a reaction kinetics model, Plasma Sources Science and Technology, 24 (2014) 015024.
[57] S.C. Saxena, S.H.P. Chen, Thermal conductivity of nitrogen in the temperature range 350–2500 K, Molecular Physics, 29 (1975) 1507-1519.
[58] V. Kotov, P.M.J. Koelman, Plug flow reactor model of the plasma chemical conversion of CO2, Plasma Sources Science and Technology, 28 (2019) 095002.
[59] S.G. Penoncello, Thermal Energy Systems : Design and Analysis, DOI (2015).
[60] V. Vermeiren, A. Bogaerts, Plasma-Based CO2 Conversion: To Quench or Not to Quench?, The Journal of Physical Chemistry C, 124 (2020) 18401-18415.
[61] J.P. Boeuf, E.E. Kunhardt, Energy balance in a nonequilibrium weakly ionized nitrogen discharge, Journal of Applied Physics, 60 (1986) 915-923.
[62] C. Gorse, M. Capitelli, Coupled electron and excited-state kinetics in a nitrogen afterglow, Journal of Applied Physics, 62 (1987) 4072-4076.
[63] V. Guerra, P.A. Sá, J. Loureiro, Kinetic modeling of low-pressure nitrogen discharges and post-discharges, Eur. Phys. J. Appl. Phys., 28 (2004) 125-152.
[64] N.A. Popov, Associative ionization reactions involving excited atoms in nitrogen plasma, Plasma Physics Reports, 35 (2009) 436-449.
[65] A. Salmon, N.A. Popov, G.D. Stancu, C.O. Laux, Quenching rate of N(2P) atoms in a nitrogen afterglow at atmospheric pressure, Journal of Physics D: Applied Physics, 51 (2018) 314001.
[66] B.R.L. Galvão, J.P. Braga, J.C. Belchior, A.J.C. Varandas, Electronic Quenching in N(2D) + N2 Collisions: A State-Specific Analysis via Surface Hopping Dynamics, Journal of Chemical Theory and Computation, 10 (2014) 1872-1877.
[67] A.I. Florescu-Mitchell, J.B.A. Mitchell, Dissociative recombination, Physics Reports, 430 (2006) 277-374.
[68] Y. Wang, O. Zatsarinny, K. Bartschat, B-spline R-matrix-with-pseudostates calculations for electron-impact excitation and ionization of nitrogen, Physical Review A, 89 (2014) 062714.
[69] K. Bartschat, J. Tennyson, O. Zatsarinny, Quantum-Mechanical Calculations of Cross Sections for Electron Collisions With Atoms and Molecules, Plasma Processes and Polymers, 14 (2017) 1600093.
[70] S. Heijkers, R. Snoeckx, T. Kozák, T. Silva, T. Godfroid, N. Britun, R. Snyders, A. Bogaerts, CO2 Conversion in a Microwave Plasma Reactor in the Presence of N2: Elucidating the Role of Vibrational Levels, The Journal of Physical Chemistry C, 119 (2015) 12815-12828.
[71] L.L. Alves, A. Bogaerts, V. Guerra, M.M. Turner, Foundations of modelling of nonequilibrium low-temperature plasmas, Plasma Sources Science and Technology, 27 (2018) 023002.
[72] A. Tejero-del-Caz, V. Guerra, D. Gonçalves, M.L. da Silva, L. Marques, N. Pinhão, C.D. Pintassilgo, L.L. Alves, The LisbOn KInetics Boltzmann solver, Plasma Sources Science and Technology, 28 (2019) 043001.
[73] R.B. Bird, W.E. Stewart, E.N. Lightfoot, Transport Phenomena, Wiley2006.
[74] H.W. Ellis, M.G. Thackston, E.W. McDaniel, E.A. Mason, Transport properties of gaseous ions over a wide energy range. Part III, Atomic Data and Nuclear Data Tables, 31 (1984) 113-151.
[75] M. Moisan, C.M. Ferreira, Y. Hajlaoui, D. Henry, J. Hubert, R. Pantel, A. Ricard, Z. Zakrzewski, Properties and applications of surface wave produced plasmas, Revue de Physique Appliquée, 17 (1982) 707-727.
[76] C.M. Ferreira, M. Moisan, Microwave Discharges: Fundamentals and Applications, Springer US2013.
[77] J. Margot, M. Moisan, Characteristics of surface-wave propagation in dissipative cylindrical plasma columns, Journal of Plasma Physics, 49 (1993) 357-374.
[78] E. Bloyet, P. Leprince, M.L. Blasco, J. Marec, Ionization by a pulsed plasma surface wave, Physics Letters A, 83 (1981) 391-392.
[79] C.M. Ferreira, Theory of a plasma column sustained by a surface wave, Journal of Physics D: Applied Physics, 14 (1981) 1811-1830.
[80] F.F. Chen, J.P. Chang, Lecture Notes on Principles of Plasma Processing, Springer US2012.
[81] J.D. Huba, D.L. Book, N.R. Laboratory, NRL Plasma Formulary, Naval Research Laboratory1998.
[82] H. Zhong, M.N. Shneider, M.S. Mokrov, Y. Ju, Thermal-chemical instability of weakly ionized plasma in a reactive flow, Journal of Physics D: Applied Physics, 52 (2019) 484001.
[83] S. Kelly, J.A. Sullivan, CO 2 Decomposition in CO 2 and CO 2 /H 2 Spark-like Plasma Discharges at Atmospheric Pressure, ChemSusChem, DOI 10.1002/cssc.201901744(2019).

[84] N. Pinhão, A. Moura, J.B. Branco, J. Neves, Influence of gas expansion on process parameters in non-thermal plasma plug-flow reactors: A study applied to dry reforming of methane, International Journal of Hydrogen Energy, 41 (2016) 9245-9255.
[85] R. Snoeckx, S. Heijkers, K. Van Wesenbeeck, S. Lenaerts, A. Bogaerts, CO2 conversion in a dielectric barrier discharge plasma: N2 in the mix as a helping hand or problematic impurity?, Energy & Environmental Science, 9 (2016) 999-1011.
[86] C.E. Treanor, J.W. Rich, R.G. Rehm, Vibrational Relaxation of Anharmonic Oscillators with Exchange-Dominated Collisions, The Journal of Chemical Physics, 48 (1968) 1798-1807.